JOURNAL OF COMPUTATIONAL PHYSICS 27, 363–396 (1978)

Hybrid Simulations of Quasineutral Phenomena in Magnetized Plasma*

J. A. BYERS, B. I. COHEN, W. C. CONDIT, AND J. D. HANSON

Lawrence Livermore Laboratory, University of California, Livermore, California 94550

Received April 27, 1977; revised July 8, 1977

Presented is a new class of numerical algorithms for computer simulation of low frequency ($\omega \ll \omega_{pe}$, ω_{ce}) electromagnetic and electrostatic phenomena in magnetized plasma. Maxwell's equations are solved in the limits of negligible transverse displacement current (Darwin's model) and quasineutrality. The numerical models treat electrons as a massless fluid and ions as particles. The numerical stability of the algorithms is investigated analytically and verified by computer experiments. The numerical algorithms, in both linearized and fully nonlinear forms, are successfully applied to the study of linear microinstabilities and the efficiency of injected small amplitude currents in causing the local reduction of the external magnetic field in magnetically confined plasmas.

1. INTRODUCTION

For many years there has been considerable motivation for generating numerical algorithms for the purpose of simulating collective plasma behavior on time scales which are long compared to the electron plasma wave and electron cyclotron periods. In magnetically confined plasmas of interest for controlled fusion, the characteristic frequencies and rates associated with radiation and relativistic effects are commonly many orders of magnitude larger than the frequencies of important microinstabilities which determine the efficiencies of particle and energy confinement. Furthermore, the fueling and heating of fusion plasmas with either neutral beam injection or electromagnetic waves typically occur on the long time scales governing confinement. To economically study the influence of these slow processes on plasma equilibrium via computer simulation requires techniques which dispense with high frequency phenomena without compromising the validity and accuracy of the simulated physics at low frequency.

In our studies we wish to correctly describe the physics of collective plasma behavior in a regime of frequencies much less than the electron cyclotron frequency ω_{ce} and plasma frequency ω_{pe}. We therefore neglect radiation and relativistic effects and solve Maxwell's equations in the Darwin approximation [1-2]. The transverse component of the displacement current is set equal to zero, and effects which are second

* Work performed under the auspices of the U.S. Energy Research and Development Administration under Contract No. W-7405-Eng-48.

0021-9991/78/0273-0363$02.00/0

order in the particle velocities over the speed of light are ignored. Furthermore, we make the assumption of quasineutrality: only long wavelength, low frequency phenomena with negligible associated space charge are allowed. We make these approximations and assumptions in the same manner and spirit as they are made in analytical theory. Our simulations are therefore only models of a restricted class of collective plasma phenomena.

Electrons are simulated as a fluid and ions as particles. When simulating with particles which are necessarily limited in number, the fluctuation levels for charge and current densities are generally much higher in simulation than in a real plasma [3]. By suppressing the normal modes associated with high frequency electromagnetic and electrostatic waves, we avoid the potential difficulty of thermally excited high frequency and short wavelength modes artifically distorting or obscuring the important physics at lower frequency and longer wavelength.

There has recently been considerable interest in hybrid (fluid and particle) and nonradiative electromagnetic simulations. An excellent review article has been written by Nielson and Lewis [4] on nonradiative electromagnetic particle simulation codes. Examples of prior work on nonradiative electromagnetic models which include electrostatic phenomena are the one-dimensional sheet model of Hasegawa and Okuda [5] and the one-dimensional finite-sized particle model of Haber *et al.* [6]. Busnardo-Neto *et al.* [7] have produced one- and two-dimensional, magnetostatic, finite-sized-particle codes. All of these codes are fully electrostatic, i.e., they solve Poisson's equation for the electrostatic potential.

More recently Nielson *et al.* [8] have constructed a quasineutral hybrid model for nonradiative electromagnetic simulation in several dimensions. In their model the transverse and longitudinal fields are constructed from iterative solution of coupled elliptic equations involving the self-consistent moments of the ion velocity distribution function and similar quantities characterizing the electron fluid. Quasineutrality requires the replacement of Poisson's equation with some other constitutive relation for the electrostatic field, in this case a generalized Ohm's law in which electron inertia effects are retained in the divergence-free part of the equation.

Our own work most closely resembles that of Nielson, Winske, and Hewett. However, we choose to examine phenomena generally at lower frequency than the lower hybrid frequency and therefore neglect electron inertia altogether. Our numerical differencing scheme differs dramatically. Instead of a generalized Ohm's law we utilize the equation of motion for the electron fluid. We present new multidimensional algorithms which are fairly direct, time-centered, and stable. Friedman *et al.* [9] have used yet another hybrid simulation model to study field-reversing proton rings in an axisymmetric cylindrical configuration.

Many previous researchers [4-7] have emphasized that direct numerical solution of Maxwell's equations in the Darwin approximation and the particle equations of motion can lead to violent numerical instability. The nonradiative approximation eliminates retardation effects in the electromagnetic fields and changes the system of equations from hyperbolic to elliptic [4]. In some sense the speed of light becomes infinite, and there is instantaneous action at a distance in the electromagnetic fields.

Numerical difficulties arise from the time derivative of the magnetic field in Faraday's law, $\nabla \times \mathbf{E} = -c^{-1}\partial \mathbf{B}/\partial t$. These problems have generally caused nonradiative codes to be much more complex than fully electromagnetic ones, and make generalization from one to two dimensions nontrivial. In view of these considerations our algorithms are remarkably simple.

Because of the introductory nature of this paper, we have restricted the applications presented here to linear phenomena. This has allowed us to compare the results of simulations using both linearized and fully nonlinear algorithms with linear analytical theory in all cases. However, to establish the real value of the new algorithms introduced here, simulations of fully nonlinear phenomena must be conducted. These are in progress and will be presented in future publications.

We have successfully applied our simulation models to the studies of small amplitude, low frequency waves ($\omega \sim \omega_{ci}$) driven unstable by non-Maxwellian velocity distribution functions or plasma gradients, e.g., unstable ion Bernstein waves [10], Alfvén-ion-cyclotron waves [11], and drift-cyclotron-loss-cone modes [12, 13]. We have also studied the effects of small amplitude injected currents on magnetic field cancellation, with the eventual goal of investigating field-reversed configurations. Although most of these examples are of particular interest to the study of fusion plasmas confined by magnetic mirrors, our simulation models can be more generally applied. In all cases however, use of these models demands that the phenomena to be studied are in fact physically decoupled from the physics we have omitted: the plasma parameters, frequencies, and wavelengths of the collective behavior simulated must be consistent with the neglect of radiation, charge separation, and electron inertia.

The paper is organized as follows. Section 2 introduces algorithms for use in one or more dimensions. An important distinction arises concerning whether or not the conservation of canonical momentum in a particular direction is utilized. In this section we also review the concept of linearized particle codes. Section 3 presents an analysis of the numerical stability of the various algorithms. We calculate the spatial and temporal mesh corrections to the linear dispersion relations describing wave propagation in a homogeneous plasma. Section 4 describes the linearized simulation of three microinstabilities: ion Bernstein waves driven unstable by a non-Maxwellian velocity distribution function (Dory-Guest-Harris instability), drift-cyclotron-loss-cone instability in the local approximation, and the Alfvén-ion-cyclotron instability. The use of injected currents to produce local magnetic field cancellation in high-β plasmas is investigated and discussed in Section 5. Section 6 concludes the paper with a brief summary and offers an overview of expected applications and future extensions of these simulation models.

2. Simulation Models

In this section we introduce a class of new algorithms for performing hybrid simulations of quasineutral, nonradiative electrostatic and electromagnetic

phenomena in magnetized plasma. The first algorithm we introduce makes use of conservation of canonical momentum and special features peculiar to the case of one-dimensional spatial variation. For the more general case in which canonical momentum is not necessarily conserved, a second closely related simulation model is offered which allows for spatial variation in several dimensions. These algorithms are also implemented in linearized form in which the current and charge density source terms in Maxwell's equations and the equations of motion for the charged particles are linearized. We thus consider linearized and fully nonlinear versions of our new algorithms.

In Coulomb gauge ($\nabla \cdot \mathbf{A} = 0$) Ampere's law becomes in the Darwin approximation

$$-\nabla^2 \mathbf{A} = 4\pi c^{-1} \mathbf{J}^t. \tag{1}$$

A superscript $t(l)$ designates the divergence (curl)-free part of a vector quantity. The magnetic field is given by $\mathbf{B} = \nabla \times \mathbf{A}$. A statement of quasineutrality can be given by taking the difference of the electron and ion continuity equations and setting $n_i \approx n_e$ to obtain

$$\nabla \cdot (\mathbf{J}_i + \mathbf{J}_e) = 0. \tag{2}$$

If the normal component of $(\mathbf{J}_i + \mathbf{J}_e)^l$ vanishes along the system boundaries (isolated plasma), then $(\mathbf{J}_i + \mathbf{J}_e)^l$ vanishes everywhere in the plasma as a consequence of Eq. (2) Equation (1) becomes $-\nabla^2 \mathbf{A} = 4\pi c^{-1} \mathbf{J}$, and separation of the currents into longitudinal and transverse parts is unnecessary. The transverse electric field and hence inductive effects are derived from Faraday's law,

$$\mathbf{E}^t = -c^{-1}\, \partial \mathbf{A}/\partial t. \tag{3}$$

Equations (1) and (3) only describe the transverse (electromagnetic) fields. Prescriptions are still required for the electrostatic field $\mathbf{E}^l$ and the motions of the electrons and ions in order to construct charge and current density source terms. We consider a simple fluid model for the electrons,

$$n_e m_e[(\partial/\partial t) + \mathbf{V}_e \cdot \nabla]\, \mathbf{V}_e = n_e q_e(\mathbf{E} + \mathbf{V}_e \times \mathbf{B}c^{-1}) + n_e m_e(\mathbf{V}_i - \mathbf{V}_e)\, \nu_{ei} - \nabla \cdot \mathbf{P}_e\,, \tag{4}$$

where $\mathbf{V}_s$ are the fluid velocities of each species, ν_{ei} is the classical electron–ion collision frequency, and $\mathbf{P}_e$ is the electron fluid pressure tensor. We now make an approximation appropriate for long wavelength, low frequency, quasineutral phenomena: we ignore electron polarization effects and inertia on the l.h.s. of Eq. (4). We solve Eq. (4) for the electric field using $\mathbf{V}_s = \mathbf{J}_s/q_s n_s$, $n_e \approx n_i$, and from Eq. (1), $\mathbf{J}_e = -(c/4\pi)\, \nabla^2 \mathbf{A} - \mathbf{J}_i$:

$$\mathbf{E} = -\omega_{pi}^{-2} c\, \nabla^2 \mathbf{A} \times \boldsymbol{\omega}_{ci} - (n_i q_i c)^{-1}\, \mathbf{J}_i \times \mathbf{B} - (n_i q_i)^{-1}\, \nabla \cdot \mathbf{P}_e - \nu_{ei} \omega_{pe}^{-2} c\, \nabla^2 \mathbf{A}, \tag{5}$$

where $\omega_{ps}^2 \equiv 4\pi n_s e^2/m_s$ and $\boldsymbol{\omega}_{ci} \equiv (q_i/m_i c)\mathbf{B}$. The electric field $\mathbf{E}$ must be separated into longitudinal and transverse parts, which in general requires solution of a Poisson's equation. An appropriate equation of state must be employed for $\mathbf{P}_e$. The system of equations is then closed by integrating equations of motion for particle ions from whose positions and velocities n_i and $\mathbf{J}_i$ are constructed:

$$d\mathbf{x}/dt = \mathbf{v} \tag{6a}$$

and

$$d\mathbf{v}/dt = (q_i/m_i)(\mathbf{E} + \mathbf{v} \times \mathbf{B}c^{-1}). \tag{6b}$$

For the sake of simplicity in the present discussion, we take $\nu_{ei} = \nabla \cdot \mathbf{P}_e = 0$ and the vacuum magnetic field $B_0 \neq 0$ to be uniform in x. In this limit $\mathbf{E}$ is perpendicular to $\mathbf{B}$ as determined by Eq. (5).

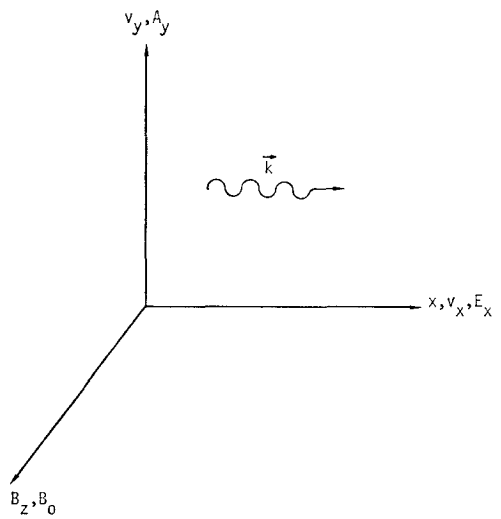

FIG. 1. One-dimensional slab coordinate system with the principal field and particle quantities shown and the direction of wave propagation indicated by **k**.

The finite-difference realization of these equations is particularly simple in one dimension. Figure 1 depicts the coordinate system for a one-dimensional simulation in which the y component of canonical momentum is conserved: $P_y \equiv m_s v_y + q_s A_y c^{-1} =$ constant. The direction of spatial variation is x, and there are velocities v_x and v_y. There are a longitudinal electric field E_x, a transverse electric field E_y, and vector potential A_y. The vacuum and self-magnetic fields point in the z direction. It is the geometrical decoupling of the transverse and longitudinal vector fields that generally makes one-dimensional versions of Darwin models especially simple.

In finite-difference form the model equations are

$$E_x(x_j)^n = -[4\pi n(x_j)^n\, e]^{-1}\, B_z(x_j)^n\, \{D^2[A_y(x_j)^n] + 4\pi c^{-1}\, J_y(x_j)^n\}, \tag{7a}$$

$$A_y(x_j)^{n+1} = A_y(x_j)^n - \Delta t\, [J_x(x_j)\, B_z(x_j)/en(x_j)]^{n+1/2}, \tag{7b}$$

$$[B_z(x_j),\, n(x_j)]^{n+1/2} = \tfrac{1}{2}[B_z(x_j)^n + B_z(x_j)^{n+1}],\ \tfrac{1}{2}[n(x_j)^n + n(x_j)^{n+1}], \tag{7c}$$

$$B_z(x_j)^n = D^1[A_y(x_j)^n] + B_0 \tag{7d}$$

for the fields, and

$$n(x_j)^n = \sum_i S(x_j - x_i{}^n), \tag{8a}$$

$$\begin{bmatrix} J_x(x_j)^{n+1/2} \\ J_y(x_j)^n \end{bmatrix} = \sum_i \begin{bmatrix} \tfrac{1}{2}[S(x_j - x_i^{n+1}) + S(x_j - x_i{}^n)]\, ev_{x,i}^{n+1/2} \\ S(x_j - x_i{}^n)\, ev_{y,i}^n \end{bmatrix}, \tag{8b}$$

$$v_{y,i}^{n+1} - v_{y,i}^0 = \sum_j (e/mc)[S(x_i{}^0 - x_j)\, A_y(x_j)^0 - S(x_i^{n+1} - x_j)\, A_y(x_j)^{n+1}$$

$$+ (x_i{}^0 - x_i^{n+1})\, B_0], \tag{8c}$$

$$v_{x,i}^{n+1/2} - v_{x,i}^{n-1/2} = \sum_j (e/m)\, \eta\, \Delta t\, S(x_i{}^n - x_j)[E_x(x_j) + v_{y,i} B_z(x_j)\, c^{-1}]^n \tag{8d}$$

$$x_i^{n+1} = x_i{}^n + \eta\, \Delta t\, v_x^{n+1/2} \tag{8e}$$

for the ion sources, where x_j are the grid locations, $S(x_i - x_j)$ is the particle shape and grid interpolation factor, η is a correction factor discussed in the next section, and D^1 and D^2 are difference operators corresponding to first and second spatial derivatives. Implicit in Eqs. (7) and (8) is that the currents, density, and velocities are those of the ions. The superscripts involving "n" denote time levels. The field equations are partially implicit as a result of the time averaging of the magnetic field in Eq. (7c) and its use in Eq. (7b). Solution of Eqs. (7b), (7c) and (7d) for $A_y(x_j)^{n+1}$ is simply performed by tridiagonal matrix inversion.

For the simulations with a spatial grid discussed in this paper we have used $D^1 f(x_j) = [f(x_{j+1}) - f(x_{j-1})]/(2\Delta x)$ and $D^2 f(x_j) = [f(x_{j+1}) - 2f(x_j) + f(x_{j-1})]/\Delta x^2$, and have employed a cloud-in-cell model and linear interpolation in evaluating $S(x - x_j)$. Care must be exercised in taking very accurate first and second derivatives of the vector potential and in using smooth particle shapes, because the vector potential is constructed from particle information without benefit of solving a Poisson equation. We are currently investigating the consequences of various particle shapes and difference operators.

Solution of Eqs. (7) and (8) requires specification of boundary conditions. Lost by our models are the physical effects associated with a plasma's collisionless skin-depth

c/ω_{pe} and Debye sheath. Since the assumption of quasineutrality and the neglect of radiation must necessarily render boundaties somewhat unphysical, we must guarantee that our boundary conditions at least imitate in some crude but reasonable way the actual physics. In any case, boundary conditions should be used which do not break the self-consistency of the numerical solution of the model equations and which do not cause the simulations to be dominated by boundary phenomena. The simplest boundary condition to implement is that of periodicity. When an ion leaves the system from one side, its motion is periodically continued on the other side. The electric and magnetic fields are also periodic to assure self-consistency. To replace the boundary condition that $\mathbf{J}^l \cdot \hat{n} = 0$ which was assumed earlier, we use $\langle \mathbf{J}^l \rangle = -(c/4\pi)(d/dt)\langle \mathbf{E}^l \rangle = 0$, where the brackets indicate the spatial average. Therefore, the implicit fluid electron current is periodic; and its longitudinal part cancels the longitudinal part of the ion current everywhere. The simulation plasma is considered to be infinite in extent, but periodic over a finite length.

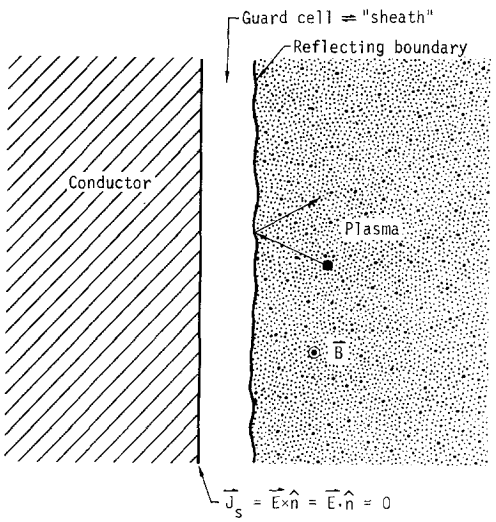

FIG. 2. Boundary conditions for simulation of a finite plasma bounded by a conducting wall. At the surface of the wall the plasma currents $\mathbf{J}_s$ identically vanish because of the presence of a particle-reflecting "sheath."

Other possible choices of consistent boundary conditions exist. Figure 2 shows one such alternative which we have successfully used. Here the plasma is bounded by a "sheath" of width equal to one grid-cell and a conducting wall. Ions are presumed to be elastically reflected by this hypothetical sheath. Since there are no plasma charges or currents in the cell nearest the wall, the electrostatic and magnetostatic self-fields of the plasma can be set equal to zero at the wall. The plasma is isolated. Within the plasma and up to the edge of the sheath, all sources and fields are otherwise calculated according to Eqs. (7) and (8). At the wall $\mathbf{A} = \mathbf{J} = \mathbf{J}^t = \mathbf{J}^l = 0$; $\mathbf{J}^l \cdot \hat{n} = 0$ is clearly satisfied, and elsewhere $\mathbf{J}_e{}^l = -\mathbf{J}_i{}^l$.

The extension of the foregoing one-dimensional, canonical-momentum-conserving algorithm to higher dimensions is not straight-forward. Difficulties arise in trying to time-center all the equations without introducing spurious effects at a frequency related to the sampling rate $\omega = \pi/\Delta t$, a common difficulty of "leap-frog" methods. For purposes of simulating a more general class of situations, we wish to relax the constraint that canonical momentum be conserved in any direction. We therefore formulate a multidimensional algorithm which is time-centered and explicit, and makes no use of the conservation of canonical momentum.

Maxwell's equations are again solved in the nonradiative and quasineutral limits with no electron polarization effects. The new scheme is given as follows:

$$\tfrac{1}{2}(\mathbf{E}^{n+1} + \mathbf{E}^n) = [-\omega_{pi}^{-2} c\, \nabla^2 \mathbf{A} \times \boldsymbol{\omega}_{ci} - (nec)^{-1}\, \mathbf{J} \times \mathbf{B} - (ne)^{-1}\, \nabla \cdot \mathbf{P}_e - \nu_{ei}\omega_{pe}^{-2} c\, \nabla^2 \mathbf{A}]^{n+1/2}, \tag{9a}$$

$$(\mathbf{E}^t = \mathbf{E} - \mathbf{E}^l)^n, \tag{9b}$$

$$\mathbf{A}^{n+1/2} = \mathbf{A}^{n-1/2} - c\, \Delta t\, \mathbf{E}^{tn}, \tag{9c}$$

$$\mathbf{B}^{n+1/2} = \nabla \times \mathbf{A}^{n+1/2} + \mathbf{B}_0\,, \qquad \mathbf{B}^n = \tfrac{1}{2}(\mathbf{B}^{n+1/2} + \mathbf{B}^{n-1/2}) \tag{9d}$$

for the fields, and

$$n(\mathbf{x}_j)^n = \sum_i S(\mathbf{x}_j - \mathbf{x}_i{}^n), \tag{10a}$$

$$n^{n+1/2} = \tfrac{1}{2}(n^n + n^{n+1}), \tag{10b}$$

$$\mathbf{J}(\mathbf{x}_j)^{n+1/2} = \sum_i \tfrac{1}{2}[S(\mathbf{x}_j - \mathbf{x}_i^{n+1}) + S(\mathbf{x}_j - \mathbf{x}_i{}^n)]\, e\mathbf{v}_i^{n+1/2}, \tag{10c}$$

$$\mathbf{v}_i^{n+1/2} - \mathbf{v}_i^{n-1/2} = \sum_j (e/m)\, \Delta t\, S(\mathbf{x}_i{}^n - \mathbf{x}_j)[\mathbf{E}(\mathbf{x}_j)^n + \tfrac{1}{2}(\mathbf{v}_i^{n+1/2} + \mathbf{v}_i^{n-1/2}) \times \mathbf{B}(\mathbf{x}_j)^n\, c^{-1}], \tag{10d}$$

$$\mathbf{x}_i^{n+1} - \mathbf{x}_i{}^n = \Delta t\, \mathbf{v}_i^{n+1/2} \tag{10e}$$

for the ion density, current, velocities and positions. Equation (10d) is solved for $\mathbf{v}_i^{n+1/2}$ by use of Boris' method [15].

In Eq. (9) the spatial mesh and the various difference operators approximating $\nabla^2, \nabla, \nabla\times$, and $\nabla\cdot$ must be consistently defined. To guarantee that gauge properties are preserved by the numerical scheme, the difference operators should be constructed so that $\nabla \cdot \nabla \times \mathbf{A} \equiv 0$ and $\nabla \times \nabla\phi \equiv 0$ to the order of the computer round-off error [8, 16]. The separation of the electric field into longitudinal and transverse components requires in general the solution of a Poisson's equation for the electrostatic potential with the source term given by $\nabla \cdot \mathbf{E}$, except for the one-dimensional case where these components are geometrically decoupled. For many systems use of a fast Fourier transform is especially conveneient for calculating $\mathbf{E}^t$ and $\mathbf{E}^l$:

$$\mathbf{E}^t = \mathbf{E} - \sum_{\mathbf{k}} \mathbf{k}(\mathbf{k} \cdot \mathbf{E}_{\mathbf{k}})\, k^{-2} \exp(i\mathbf{k} \cdot \mathbf{x}) + \text{c.c.}$$

Appendix 1 considers a variation of the leap-frog algorithm which deals with **E** and **B** directly and dispenses with **A** and the need to separate $\mathbf{E}^t$ and $\mathbf{E}^l$.

We show in the next section that this multidimensional algorithm exhibits oscillations at frequency $\omega = \pi/\Delta t$. Because of the structure of Eq. (9a) we refer to this algorithm as the leap-frog method. A high frequency oscillation is a typical difficulty of leap-frog schemes. For illustrative purposes we introduce an implicit version of the leap-frog algorithm. Equation (9a) is replaced by

$$\mathbf{E}^n = \tfrac{1}{2}[-\omega_{pi}^{-2} c\, \nabla^2 \mathbf{A} \times \boldsymbol{\omega}_{ci} - (nec)^{-1}\, \mathbf{J} \times \mathbf{B} - (ne)^{-1}\, \nabla \cdot \mathbf{P}_e - \nu_{ei}\omega_{pe}^{-2} c\, \nabla^2 \mathbf{A}]^{n-1/2} + \tfrac{1}{2}[\qquad]^{n+1/2},$$

where the square brackets on the r.h.s. contain the same quantities but at different time levels. The rest of the implicit algorithm is as given by Eqs. (9b)–(9d) and (10). Due to the role of the particle quantities in the implicit relations for the electric and magnetic fields, this algorithm is not practical for actual computer implementation. However, the scheme is conceptually useful because of its good stability properties and elimination of all leap-frog difficulties. These advantages of the implicit method motivate yet another algorithm, which has been implemented.

A predictor-corrector version of the leap-frog algorithm set forth in Eqs. (9) and (10) offers an attractive compromise between the leap-frog and implicit schemes. Equation (9a) is used as a predictor of the electric field, $\mathbf{E}_{\text{pred}}^{n+1}$. Eqs. (9b)–(10e) then establish predicted values of **A**, $\mathbf{v}_i$, and **J** at $n + 3/2$ as well as $\mathbf{x}_i$ and ion density n at $n + 2$. The electric field at $n + 1$ is then corrected by use of

$$\mathbf{E}_{\text{corr}}^{n+1} = \tfrac{1}{2}[\qquad]^{n+1/2} + \tfrac{1}{2}[\qquad]_{\text{pred}}^{n+3/2}, \tag{11}$$

where the brackets contain the same quantities as those in Eq. (9a) evaluated at the appropriate time levels. The corrected electric field is then used to calculate new values of **A**, $\mathbf{v}_i$, and **J** at $n + 3/2$, and $\mathbf{x}_i$ and n at $n + 2$. Further corrector iterations can be performed by replacing the predictor obtained values in the second bracket appearing in Eq. (11) with the previously obtained corrected values.

We have implemented all of the foregoing algorithms except for the implicit scheme in either fully nonlinear or linearized forms. The concept and application of linearized particle codes have been discussed in Refs. [17, 18]. Linearized codes analytically separate field and source equations into equations for quantities which are zero and first order in a perturbed quantity, e.g., a small amplitude perturbation of an equilibrium electric or magnetic field. The numerical solution of the linearized equations proceeds as is outlined in the preceding for a fully nonlinear code with some important exceptions. In a linearized code one is free to follow the linear evolution of a single Fourier mode, provided that the system is infinite and uniform. In this case the spatial grid and the associated numerical effects can be eliminated. Since nonlinear effects are precluded, the linear frequency and growth or damping of a perticular Fourier mode can be observed over a very long time period and therefore measured quite accurately. Linearized codes are useful for testing and calibrating basic numerical

algorithms because they ease the direct comparison of simulation results with linear analytical theory. These codes are also being currently used to study the linear stability of complex equilibria which are intractable to analytical treatment, for example equilibria in which finite plasma and Larmor radius effects are important.

3. Numerical Stability Analysis

To determine the numerical stability properties of the various algorithms introduced we analyze the linear dispersion relations describing the propagation of small amplitude waves, including effects due to finite-differencing and finite-sized particles. We begin by considering the simple case of a cold plasma for which we establish the conditions for the stable propagation of compressional Alfvén waves. The relative simplicity of the physics of wave propagation perpendicular to a uniform magnetic field in cold homogeneous plasma allows easy clarification of the differences between the numerical methods. Analytical theory is presented for our algorithms and, where possible, theory is compared with numerical simulations. This section is concluded with an analysis applied to the one-dimensional, canonical momentum conserving algorithm for the more general case of a warm plasma.

We begin by considering the one-dimensional scheme which assumes conservation of canonical y momentum. Finite Fourier transforms are represented as follows:

$$(E_x, A_y, \ldots) = (\tilde{E}_x, \tilde{A}_y, \ldots) \exp(i\omega t + ikx) + c.c.$$

The Fourier transformed difference operators for the standard centered two-point and three-point operators are given by $\tilde{D}^1 = ik \sin(k\,\Delta x)/(k\,\Delta x)$ and $\tilde{D}^2 \equiv -K^2 = -k^2 \sin^2(k\,\Delta x/2)/(k\,\Delta x/2)^2$. Because the Fourier transformed shape factor using linear weighting, $\tilde{S} = \sin^2(k\,\Delta x/2)/(k\,\Delta x/2)^2$, decreases fairly rapidly, contributions to the particle currents at spatially aliased short wavelengths ($k\,\Delta x > \pi$) are small. We neglect the spatial aliases in our analysis but emphasize that in some cases they are very important [3]. This approximation is justified a posteriori by the excellent agreement of the predictions of the following analytical theory with computer simulations.

We linearize and Fourier transform Eqs. (7) and (8),

$$\tilde{E}_x = (Kc/\omega_{pi})^2\, \omega_{ci}\, c^{-1}\, \tilde{A}_y - \tilde{S}(m/e)\, \omega_{ci}\, \tilde{v}_y\,, \tag{12a}$$

$$i \sin(\omega\,\Delta t/2)(c\,\Delta t)^{-1}\, \tilde{A}_y = \tilde{S}(m/e)\, \omega_{ci} \tilde{v}_x\,, \tag{12b}$$

$$\tilde{v}_y = -\tilde{S}(e/mc)\, \tilde{A}_y - \omega_{ci}\tilde{x}, \tag{12c}$$

$$\tilde{v}_x = i\eta\, (\omega_{ci}\, \Delta t/2)[\sin(\omega\,\Delta t/2)]^{-1}\, (\tilde{S}\tilde{E}_x B^{-1} c + \tilde{v}_y), \tag{12d}$$

$$\tilde{x} = i\eta(\tilde{v}_x\, \Delta t/2)[\sin(\omega\,\Delta t/2)]^{-1}. \tag{12e}$$

The factor η [$= \sin(\omega_{ci}\,\Delta t/2)/(\omega_{ci}\,\Delta t/2)$] insures that the ions gyrate with correct

cyclotron frequency (see the Appendix). Equations (12) are algebraically reduced to give

$$\begin{bmatrix} \eta \dfrac{\tilde{S}^2 \omega_{ci}\, \Delta t/2}{\sin(\omega\, \Delta t/2)} & \eta(\eta - \tilde{S}^2) \dfrac{\omega_{ci}\, \Delta t/2}{\sin(\omega\, \Delta t/2)} - \dfrac{\sin(\omega\, \Delta t/2)}{\omega_{ci}\, \Delta t/2} \\ 1 + (\tilde{S}^2 - 1)\, \eta^2 \dfrac{(\omega_{ci}\, \Delta t/2)^2}{\sin^2(\omega\, \Delta t/2)} & -\left\{ \dfrac{K^2 c^2}{\omega_{pi}^2} \left[1 - \dfrac{\eta^2 (\omega_{ci}\, \Delta t/2)^2}{\sin^2(\omega\, \Delta t/2)} \right] + \tilde{S}^2 \right\} \end{bmatrix} \begin{bmatrix} \dfrac{\tilde{E}_x c}{B_0} \\ \dfrac{e\tilde{A}_y}{mc} \end{bmatrix} = 0. \tag{13}$$

We set the determinant of the matrix in Eq. (13) equal to zero to obtain a biquadratic dispersion relation for $\sin(\omega\, \Delta t/2)$. There are two simple limiting cases which correspond to the numerical simulations we have performed. For gridless linearized simulations ($\Delta x = 0$) the normal mode frequencies are given by

$$\sin^2(\omega\, \Delta t/2) = \eta k^2 {V_A}^2\, \Delta t^2/4,\ \eta^2 \omega_{ci}^2\, \Delta t^2/4, \tag{14}$$

where $V_A = (\omega_{ci}/\omega_{pi})\, c$, the usual Alfvén velocity. With a spatial grid and $\eta \equiv 1$, one obtains

$$\sin^2(\omega\, \Delta t/2) = \tilde{S}^2 K^2 {V_A}^2\, \Delta t^2/4,\ [1 + (1 - \tilde{S}^2)^2]\, \omega_{ci}^2\, \Delta t^2/4. \tag{15}$$

In both cases the two solutions of the dispersion relation correspond to the compressional Alfvén wave and the cold plasma ion-cyclotron resonance. The relative polarization of the fields is deduced by taking the ratio of the appropriate matrix elements in Eq. (13); for $\eta \approx \tilde{S} \approx 1$, $\tilde{E}_x/\tilde{E}_y \approx i \sin(\omega\, \Delta t/2)/(\omega_{ci}\, \Delta t/2)$.

Stable wave propagation results when the r.h.s. of Eqs. (14) and (15) are less than unity, viz.

$$(kV_A\, \Delta t/2)_{\text{eff}}^2,\ (\omega_{ci}\, \Delta t/2)_{\text{eff}}^2 < 1, \tag{16}$$

where the effective values of the Alfvén velocity and the cyclotron frequency are defined as having absorbed the appropriate combinations of η and $\tilde{S}^2$ factors. Numerical instability results when the r.h.s. of Eqs. (14) and (15) exceed unity.

Figure 3 shows the results of numerical simulations in which small amplitude compressional Alfvén waves were excited. The dashed line indicates the theoretical dispersion relation with $\Delta x \equiv \Delta t \equiv 0$, while the solid curve gives the dispersion relation including both finite Δt and Δx. Data were obtained from both a fully nonlinear code with $\eta \equiv 1$ and $k\, \Delta x = \pi/4$, and a linearized gridless code with $\eta \equiv \sin(\omega_{ci}\, \Delta t/2)/(\omega_{ci}\, \Delta t/2)$. A broad range of values of $\omega_{ci}\, \Delta t/2$ was employed: $0.01 \leqslant \omega_{ci}\, \Delta t/2 \leqslant \pi/2$. We observe excellent agreement between the finite-difference modified theory for the algorithm employing conservation of canonical momentum and the results of simulation over the entire range of frequencies and wavenumbers giving numerically stable propagation. Numerical dispersion becomes appreciable only for $kV_A\, \Delta t/2 \to 1$. We have also verified that the electric field polarization of the waves and the onset of numerical instability are consistent with theory.

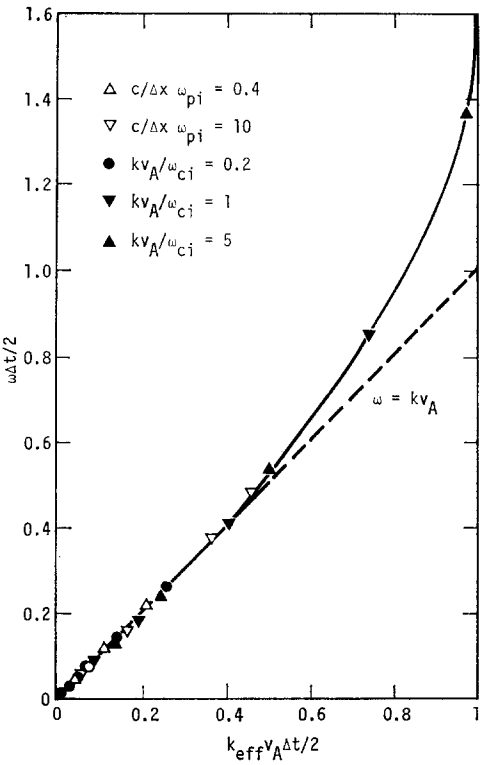

FIG. 3. Theoretical dispersion relation for compressional Alfvén waves with space-time mesh corrections as deduced for the canonical-momentum-conserving algorithm. The dashed line is for $\Delta x = \Delta t = 0$; the solid curve includes the modifications due to finite differencing and is the solution of $\sin^2(\omega\Delta t/2) = (k_{eff}V_A\Delta t/2)^2$, where $k_{eff} \equiv \eta^{1/2}k$ for $\Delta x = 0$ (linearized simulation) and $k_{eff} \equiv \tilde{S}\,k$ for $\Delta x \neq 0$ (fully nonlinear). Simulation data are shown in solid symbols for $\Delta x = 0$ and open symbols for $\Delta x \neq 0$.

Our more general multidimensional algorithms can be analyzed similarly. Again we consider one-dimensional wave propagation perpendicular to a uniform magnetic field in a cold homogeneous plasma. For the coordinate system shown in Fig. 1, the linearized equations described Fourier amplitudes derived from Eqs. (9) and (10) are

$$\cos(\omega\,\Delta t/2)\,\tilde{E}_x = -\omega_{ci}(m/e)[i(Kc/\omega_{pi})^2\,(e/m)(\Delta t/2)\sin^{-1}(\omega\,\Delta t/2)\,\tilde{E}_y + \tilde{S}\tilde{v}_y], \quad (17a)$$

$$\cos(\omega\,\Delta t/2)\,\tilde{E}_y = \omega_{ci}(m/e)\,\tilde{S}\tilde{v}_x\,, \quad (17b)$$

$$i(c\,\Delta t/2)^{-1}\sin(\omega\,\Delta t/2)\,\tilde{A}_y = \tilde{E}_y\,, \quad (17c)$$

$$-i\sin(\omega\,\Delta t/2)\,\tilde{v}_x = (\omega_{ci}\,\Delta t/2)\cos(\omega\,\Delta t/2)\,\tilde{v}_y + (e/m)(\Delta t/2)\,\tilde{S}\tilde{E}_x\,, \quad (17d)$$

$$-i\sin(\omega\,\Delta t/2)\,\tilde{v}_y = -(\omega_{ci}\,\Delta t/2)\cos(\omega\,\Delta t/2)\,\tilde{v}_x + (e/m)(\Delta t/2)\,\tilde{S}\tilde{E}_y\,. \quad (17e)$$

Algebraic reduction of these equations gives

$$\begin{bmatrix} \tilde{S}^2 & D_{xy} = i\dfrac{\tan(\omega\,\Delta t/2)}{\omega_{ci}\,\Delta t/2}\left\{\cos^2(\omega\,\Delta t/2) + \dfrac{(\omega_{ci}\,\Delta t/2)^2}{\tan^2(\omega\,\Delta t/2)}\left[S^2 - \cos^2(\omega\,\Delta t/2)\right]\right\} \\ D_{xy} = -D_{xy} & \dfrac{K^2c^2}{\omega_{pi}^2}\left[1 - \dfrac{(\omega_{ci}\,\Delta t/2)^2}{\tan^2(\omega\,\Delta t/2)}\right] + \tilde{S}^2 \end{bmatrix} \begin{bmatrix} \tilde{E}_x \\ \tilde{E}_y \end{bmatrix} = 0. \quad (18)$$

Setting the determinant of the matrix in Eq. (18) equal to zero yields a cubic equation for $\tan^2(\omega\,\Delta t/2)$. For sake of simplicity we consider the limit $k\,\Delta x \to 0$. We obtain the following dispersion relation

$$\frac{k^2c^2}{\omega_{pi}^2}(y-1)(1+y\omega_{ci}^2\,\Delta t^2/4) + y(1+y\omega_{ci}^2\,\Delta t/4)^2 - y^2(1+\omega_{ci}^2\,\Delta t^2/4)^2 = 0, \quad (19)$$

where $y \equiv \tan^2(\omega\,\Delta t/2)/(\omega_{ci}\,\Delta t/2)^2$. For $\omega_{ci}\,\Delta t/2 \ll 1$ there exist the approximate solutions

$$\tan^2(\omega\,\Delta t/2) \approx \begin{cases} (kV_A\,\Delta t/2)^2, & (\omega_{ci}\,\Delta t/2)^2 \ll 1, \\ (1 + k^2c^2/\omega_{pi}^2)^{-1}\,(\omega_{ci}\,\Delta t/2)^{-2} \gg 1. \end{cases} \quad (20)$$

Thus there is an extra branch at high frequency ($\omega \approx \pm\pi/\Delta t$). This illustrates the chief numerical problem of the leap-frog algorithm. The extra branch emerged in our linearized simulations of compressional Alfvén waves in cold plasma (Fig. 4) as a stable oscillation at one-half the sampling frequency for choice of time steps such that $kV_A\,\Delta t$, $\omega_{ci}\,\Delta t/2 < 1$. Simulations demonstrated that with increasing $kV_A\,\Delta t$ the phase velocity of the compressional Alfvén waves increased, $\omega/k > V_A$, until onset of instability. Simulations using the leap-frog algorithm were numerically unstable for $kV_A\,\Delta t$ (or $\omega_{ci}\,\Delta t/2) \gtrsim 1$.

The implicit algorithm resolves the difficulties of the leap-frog scheme by performing the temporal average on the r.h.s. of Eq. (9a) instead of the l.h.s. The $\cos(\omega\,\Delta t/2)$ factors on the l.h.s. of Eqs. (17a) and (17b) now appear on the r.h.s., In place of Eq. (18) we obtain

$$\begin{bmatrix} \tilde{S}^2 & D_{xy} = i\dfrac{\tan(\omega\,\Delta t/2)}{\omega_{ci}\,\Delta t/2}\left[1 + \dfrac{(\omega_{ci}\,\Delta t/2)^2}{\tan^2(\omega\,\Delta t/2)}\right](\tilde{S}^2 - 1) \\ D_{xy} = -D_{xy} & \dfrac{K^2c^2}{\omega_{pi}^2}\left[1 - \dfrac{(\omega_{ci}\,\Delta t/2)^2}{\tan^2(\omega\,\Delta t/2)}\right] + \tilde{S}^2 \end{bmatrix} \begin{bmatrix} \tilde{E}_x \\ \tilde{E}_y \end{bmatrix} = 0. \quad (21)$$

This gives a biquadratic dispersion relation for $\tan(\omega\,\Delta t/2)$,

$$y^2 - [\tilde{S}^4 - (Kc/\omega_{pi})^2\,\tilde{S}^2 - 2(\tilde{S} - 1)]\,y + (Kc/\omega_{pi})^2\,\tilde{S}^2 + (\tilde{S}^2 - 1)^2 = 0, \quad (22)$$

where $y \equiv \tan^2(\omega\,\Delta t/2)/(\omega_{ci}\,\Delta t/2)^2$. Equation (22) has positive real solutions for all values of $\tilde{S}^2 \leqslant 1$ and K^2c^2/ω_{pi}^2. Equation (21) corresponds to Eq. (13) with $\eta = 1$ and

$\tan(\omega\ \Delta t/2)$ replacing $\sin(\omega\ \Delta t/2)$. The normal modes for the implicit scheme therefore have frequencies given by

$$\tan^2(\omega\ \Delta t/2) = \bar{S}^2 K^2 V_A{}^2\ \Delta t^2/4,\ [1 + (1 - \bar{S}^2)^2]\ \omega_{ci}^2\ \Delta t^2/4. \tag{23}$$

Thus the implicit algorithm is unconditionally stable and eliminates the spurious high frequency branch of the leap-frog scheme.

The impracticality of the implicit algorithm combined with its obvious advantages, as belied by Eq. (23), motivated the introduction of the predictor-corrector scheme, Eqs. (9), (10) and (11), as a compromise. The predictor-corrector algorithm was

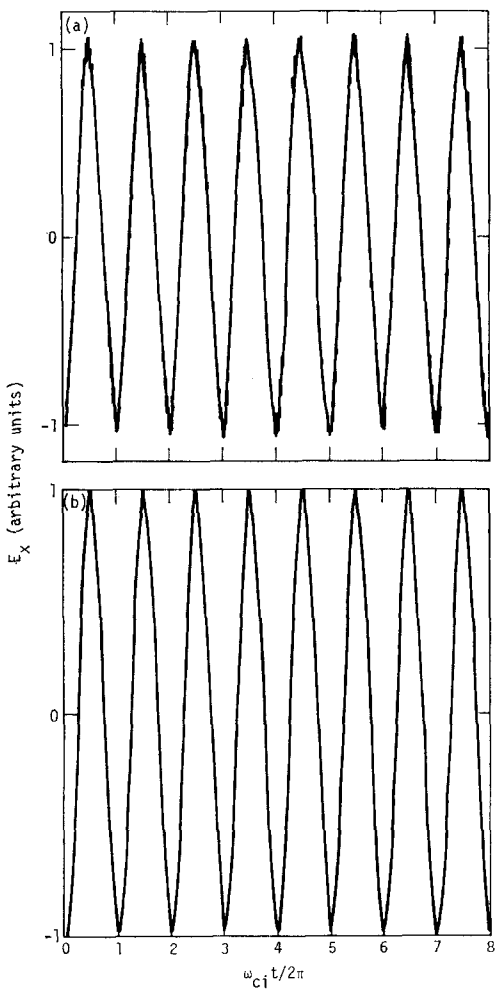

FIG. 4. Longitudinal electric field E_x verses time at a fixed position for a compressional Alfvén wave with $kV_A = \omega_{ci}$ and $\omega_{ci}\Delta t = 0.1$. Linearized simulation results using the (a) leap-frog scheme (with spurious high frequency oscillation) and (b) predictor-corrector scheme.

compared to the earlier schemes by again simulating in linearized, gridless fashion the propagation of compressional Alfvén waves. With only one full corrector iteration at each time step, high frequency oscillations were effectively extinguished; and the compressional Alfvén waves suffered some dissipation (Fig. 4). With increasing $kV_A\,\Delta t$ there was a decrease of phase velocity, $\omega/k < V_A$, and an increasing amount of numerical dissipation. The damping became severe as $kV_A\,\Delta t \to 1$, and the predictor-corrector algorithm was found to be unstable for $kV_A\,\Delta t \gtrsim 1$ or $\omega_{ci}\,\Delta t/2 \gtrsim 1$. When $\omega_{ci}\,\Delta t, kV_A\,\Delta t \leqslant 0.1$ there was little numerical dissipation and the theoretical dispersion relation for compressional Alfvén waves was reproduced by the simulations.

We finish this section by reviewing the results of a warm homogeneous plasma analysis of the one-dimensional, canonical mpmentum conserving algorithm. In Appendix 2 we extend Langdon's analysis [3] for electrostatic waves propagating perpendicular to a uniform magnetic field to include electromagnetic perturbations in the nonradiative and quasineutral limits. We continue to ignore electron inertia and temperature. For small amplitude waves propagating in the x direction and magnetic field in z we obtain

$$\begin{bmatrix} D_{xx} & D_{xy} \\ D_{yx} & D_{yy} \end{bmatrix} \begin{bmatrix} \tilde{E}_x \\ -(i\omega/c)\,\tilde{A}_y \end{bmatrix} = 0 \tag{24}$$

where

$$D_{xx} = \frac{\omega_{pi}^2}{\omega\omega_{ci}} \tilde{S}^2 \int dv_\perp\, v_\perp g_0(v_\perp) \sum_r \frac{(\eta\omega_{ci}\,\Delta t/2)}{(\eta\omega_{ci}\,\Delta t/2)^2 - \sin^2(\omega_r\,\Delta t/2)} \Big[\sin(\omega_r\,\Delta t/2)\, J_r^2 + (\eta\omega_{ci}\,\Delta t/2)\cos(\omega_r\,\Delta t/2)\,\frac{kv_\perp}{2\omega_{ci}}\, J_r(J_{r-1} + J_{r+1})\Big], \tag{25a}$$

$$D_{xy} = \frac{i\omega_{pi}^2}{\omega\omega_{ci}} \Big[\!\Big[\frac{\sin(\omega\,\Delta t/2)}{\omega\,\Delta t/2} - \tilde{S}^2 \int dv_\perp\, v_\perp g_0(v_\perp) \sum_r \frac{(\eta\omega_{ci}\,\Delta t/2)}{(\eta\omega_{ci}\,\Delta t/2)^2 - \sin^2(\omega_r\,\Delta t/2)} \times \Big\{ \frac{\omega_{ci}}{\omega} J_r^2 \sin(\omega_r\,\Delta t/2) + \frac{kv_\perp}{2\omega} \frac{\sin(k\,\Delta x)}{k\,\Delta x} (J_{r+1}J_r - J_{r-1}J_r)\sin(\omega_r\,\Delta t/2) + (\eta\omega_{ci}\,\Delta t/2)\cos(\omega_r\,\Delta t/2)\,\frac{kv_\perp}{2\omega_{ci}} \Big[\frac{kv_\perp}{2\omega} \sin\frac{(k\,\Delta x)}{k\,\Delta x} (J_{r+1} - J_{r-1}) \times (J_{r+1} + J_{r-1}) + \frac{\omega_{ci}}{\omega} J_r(J_{r-1} + J_{r+1})\Big]\Big\}\Big]\!\Big], \tag{25b}$$

$$D_{yx} = \frac{i\omega_{pi}^2}{\omega\omega_{ci}} \Big\{1 - \int dv_\perp\, v_\perp g_0(v_\perp) \sum_r \frac{(\eta\omega_{ci}\,\Delta t/2)^2\,\tilde{S}^2}{(\eta\omega_{ci}\,\Delta t/2)^2 - \sin^2(\omega_r\,\Delta t/2)} \times \Big\{J_r^2 + \frac{kv_\perp}{2\omega_{ci}} J_r(J_{r-1} - J_{r+1})\Big]\Big\}, \tag{25c}$$

$$D_{yy} = \frac{K^2c^2}{\omega^2} + \frac{\omega_{pi}^2}{\omega\omega_{ci}} \tilde{S}^2 \int dv_\perp v_\perp g_0(v_\perp) \sum_r \left[\left[\frac{\omega_{ci}}{\omega} J_r^2 - \frac{(\eta\omega_{ci}\,\Delta t/2)^2}{(\eta\omega_{ci}\,\Delta t/2)^2 - \sin^2(\omega_r\,\Delta t/2)} \right.\right.$$
$$\times \left\{ \frac{\omega_{ci}}{\omega} J_r^2 + \frac{kv_\perp}{2\omega} \frac{\sin(k\,\Delta x)}{k\,\Delta x} J_r(J_{r+1} - J_{r-1}) \right.$$
$$\left.\left. - \frac{kv_\perp}{2\omega} \left[J_rJ_{r-1} - J_rJ_{r+1} - \frac{kv_\perp}{2\omega_{ci}} \frac{\sin(k\,\Delta x)}{k\,\Delta x} (J_{r+1} - J_{r-1})^2 \right] \right\} \right], \tag{25d}$$

$g_0(v_\perp)$ is the normalized distribution function for perpendicular velocities, $\omega_r \equiv \omega - r\Omega$ where $\sin(\Omega\,\Delta t/2) = \eta\omega_{ci}\,\Delta t/2$, and the argument of the Bessel functions $J_r(\chi)$ is given by $\chi \equiv kv_\perp/\Omega$. Use of the identities

$$\sin(\omega_1\,\Delta t)[\sin^2(\omega_2\,\Delta t/2) - \sin^2(\omega_1\,\Delta t/2)]^{-1} = \cot[(\omega_2 - \omega_1)\,\Delta t/2] - \cot[(\omega_2 + \omega_1)\,\Delta t/2],$$
$$[J_{r-1}(\chi) + J_{r+1}(\chi)]^2 = (4r^2/\chi^2)\,J_r(\chi)^2,$$
$$J_{r+1}(\chi)^2 - J_{r-1}(\chi)^2 = -(2r/\chi)(d/d\chi)\,J_r(\chi)^2$$

allows some simplification of the matrix elements, Eqs. (25), but is unnecessary for purposes of the present discussion. We have again ignored contributions from spatial aliases.

The dispersion relation describing normal modes in the periodic simulation plasma is then given by $\det \mathbf{D} = D_{xx}D_{yy} - D_{xy}D_{yx} = 0$. Due to the finite ion temperature, the cold plasma resonance at $\pm\omega_{ci}$ is replaced by the entire ion Bernstein spectrum and its cutoffs and resonances at all ion cyclotron harmonics. The compressional Alfvén wave remains purely transverse for $|\,\omega/\omega_{ci}\,| \ll 1$ but is modified by thermal effects. The coupling of the electromagnetic and electrostatic branches becomes important for finite values of $k\,\langle v_\perp\rangle/\omega_{ci}$ and $\omega_{pi}^4/\omega_{ci}^2k^2c^2$[19]. Callen and Guest [19] have described the electromagnetic modifications to certain electrostatic modes. They analyze in what circumstances the Bessel function series in D_{xy} and D_{yx} are small compared to the remaining $\mathbf{E} \times \mathbf{B}$ terms and find that it is required that $r\Omega < J_r^2(\mathbf{B}) > /(\omega - r\Omega) \ll 1$. We make this assumption and also assume that $\omega^2 \ll K^2c^2$ to obtain

$$D_{xy} \approx \frac{i\omega_{pi}^2}{\omega\omega_{ci}} \frac{\sin(\omega\,\Delta t/2)}{\omega\,\Delta t/2},$$
$$D_{yx} \approx \frac{i\omega_{pi}^2}{\omega\omega_{ci}},$$

and

$$D_{yy} \approx \frac{K^2c^2}{\omega^2}.$$

The dispersion relation for electrostatic waves then becomes

$$\tilde{S}^{-2}[D_{xx} - D_{xy}D_{yx}D_{yy}^{-1}] = \tilde{S}^{-2}D_{xx} + \frac{\omega_{pi}^4}{\tilde{S}^2K^2c^2\omega_{ci}^2} \frac{\sin(\omega\,\Delta t/2)}{\omega\,\Delta t/2} = 0. \tag{26}$$

The term $\tilde{S}^{-2}D_{xx}$ is just the linear ion susceptibility. In the quasineutral approximation the vacuum polarization term is omitted, as is the electron polarization term because of the neglect of electron inertia. Hence we can view the electromagnetic modification as merely a replacement of the vacuum term equal to unity by $[\sin(\omega\,\Delta t/2)/(\omega\,\Delta t/2)]$ $(\omega_{pi}^4/\tilde{S}^2K^2c^2\omega_{ci}^2)$. Electron polarization effects would have introduced an additional term of order $\omega_{pe}^2/\omega_{ce}^2$ [19].

Langdon [3] has analyzed how temporal aliasing of cyclotron harmonics can lead to a numerical instability for waves propagating across the magnetic field. Discrete sampling in time acts as a pump with frequency given by $2\pi/\Delta t$ which parametrically couples the electrostatic modes to themselves. However, the onset of instability is quite sensitive to frequency matching conditions, and the instability can be partially or completely stabilized by using smooth velocity distribution functions and by insuring that $\omega_{ci}\,\Delta t \ll 1$ and $\langle v_\perp\rangle/\Delta x\,\omega_{ci} \lesssim 1$ [3]. This forces the instability to occur, if at all, at high cyclotron harmonic numbers where the smallness of the associated Bessel functions in D_{xx} reduces the coupling coefficients and hence growth rates. Furthermore, even if there is instability, saturation tends in practice to occur at a fairly low level if $\omega_{ci}\,\Delta t \ll 1$ [3]. Thus our simulation algorithm can successfully avoid serious difficulties due to temporal aliasing of the cyclotron harmonics by suitable choices of time-step and distribution function.

4. Examples of Microinstabilities

This section presents examples of the application of our computer models to the study of microinstabilities. We examine three fairly simple instabilities: unstable ion Bernstein waves propagating perpendicular to a uniform magnetic field (Dory-Guest-Harris modes), the drift-cyclotron-loss-cone mode in local approximation, and the Alfvén-ion-cyclotron mode. In all cases we find agreement between the frequencies and growth rates measured in linearized simulations and those predicted by analytical theory.

1. *Dory-Guest-Harris Modes*

The Dory-Guest-Harris instability consists of Bernstein modes which are driven unstable by a non-Maxwellian velocity distribution function. The simple case of instability with a distribution function of the form $g_0(\mathbf{v}) = (2\pi v_\perp{}^0)^{-1}\,\delta(v_\perp - v_\perp{}^0)$ $\delta(v_\parallel)$ has been extensively studied by Dory *et al.* [9] and Crawford and Tataronis [20]. The dispersion relation for these modes including the lowest order electromagnetic modifications [19], but excluding vacuum and electron polarization terms, is given by Eq. (26) (with $\Delta x = \Delta t = 0$),

$$\frac{\omega_{pe}^4}{\omega_{ce}^2k^2c^2} - \frac{\omega_{pi}^2}{\omega_{ci}^2}\sum_{n=1}^{\infty}\frac{2(\partial/\partial\mu)[J_n{}^2(\mu)]}{\mu[(\omega/n\omega_{ci})^2 - 1]} = 0, \tag{27}$$

where $\mu = kv_\perp{}^0/\omega_{ci}$ and $\mathbf{k} \cdot \mathbf{B}_0 = 0$. This can be cast in the form

$$1 - \alpha \frac{\Omega}{\mu} \frac{\partial}{\partial \mu} \int_0^\pi d\Psi \frac{\cos(\Omega\Psi)\, J_0[2\mu \cos(\Psi/2)]}{\sin(\pi\Omega)} = 0,$$

where $\alpha \equiv \mu^2/\beta$, $\beta \equiv 4\pi n_0 m v_\perp^{02}/B_0{}^2$ and $\Omega \equiv \omega/\omega_{ci}$. This dispersion relation is valid in the limit of $\mu^2/\beta \ll m_i/m_e, \omega_{pi}^2/\omega_{ci}^2$. Crawford and Tataronis have obtained numerical solutions for Ω as a function of μ for various parameter values of α. (Crawford and Tataronis considered the purely electrostatic limit, in which case $\alpha \equiv \omega_{pi}^2/\omega_{ci}^2$). For a given value of wavenumber (μ), solution of Eq. (27) demonstrates that increased β is stabilizing for moderately large β, $\beta \lesssim 1$. For $\beta \gg 1$ electromagnetic and electrostatic branches become strongly coupled; Eq. (27) ceases to be valid. A more general consideration of Eq. (24) is required in which ion contributions to D_{xy}, D_{yx}, and D_{yy} in Eqs. (25) cannot necessarily be ignored. Electromagnetic ion-cyclotron waves propagating perpendicular to the magnetic field can be driven unstable in the high-β limit.

Dory-Guest-Harris modes were studied with the linearized, one-dimensional, canonical-momentum-conserving code. Finite-difference modifications to the dispersion relation, Eq. (27), are given by Eq. (26). For $\omega\, \Delta t \approx \mathcal{O}(\omega_{ci}\, \Delta t) \leqslant 0.1$, time-step effects are negligible. Because the simulation is linearized and gridless, $k\, \Delta x \to 0$, there are no spatial grid effects. Consider an example: for $\mu^2/\beta = 20$ and $\mu = 4.5$, the approximate dispersion relation Eq. (26) predicts that $\omega/\omega_{ci} = 1.28 + i\,0.45$. Linearized simulation gave $\omega/\omega_{ci} = 1.25 + i\,0.40$. For $\beta \gg 1$, unstable electromagnetic ion-cyclotron waves were observed as expected.

2. *Drift-Cyclotron-Loss-Cone-Modes*

For simulations of the drift-cyclotron-loss-cone instability, we adopt the local approximation, i.e., the density gradient is assumed constant and any variation of the mode amplitude in the direction of the density gradient is ignored. As a further simplification, we assume that the mode is a flute, $\mathbf{k} \cdot \mathbf{B}_0 = 0$ [13]; and we dispense with the self-consistent equilibrium gradient of the magnetic field. For $\Omega/\omega_{ce} \equiv (\omega + i\gamma)/\omega_{ce}$, $k_\perp a_e \ll 1$; $k_\perp a_i \gg 1$, where $a_s \equiv \langle v_{\perp s} \rangle/\omega_{cs}$; and weak gradients; the simplified dispersion relation for this mode is given by

$$\frac{\omega_{pi}^2}{k_\perp{}^2 c^2} - \frac{1}{\Omega_i k_\perp L_n} + \frac{2\omega_{ci}^3}{\pi k_\perp{}^3}\, \Omega_i \sum_n \int_0^\infty dv_\perp \frac{\partial g_{0i}/\partial v_\perp{}^2}{n + \Omega_i} = 0, \tag{28}$$

where the plasma scale length is defined as $L_n \equiv (\nabla \ln n_0)^{-1}$ and the nondimensional frequency is $\Omega_i \equiv \Omega/\omega_{ci}$. The first term on the l.h.s. of Eq. (28) is identical in origin to the $\omega_{pe}^4/(\omega_{ce} k^2 c^2) = \omega_{pi}^4/(\omega_{ci}^2 k^2 c^2)$ term in Eq. (27). These terms arise from consideration of the *electron* $\mathbf{E} \times \mathbf{B}$ motion which cross-couples electromagnetic and electrostatic field perturbations in a plasma. Vacuum and electron polarization terms have again been set equal to zero, which is consistent with our simulation model. The

drift-cone mode has frequency $\omega \sim \mathcal{O}(\omega_{ci})$ and is driven unstable by both the loss-cone in velocity space and spatial inhomogeneity.

Because of the loss of the constant vacuum and electron polarization terms, Eq. (28) does not accurately describe drift-cone modes at short wavelengths. Solution of Eq. (28) predicts that $\gamma \to \infty$ as $k_\perp \to \infty$, contrary to theory retaining the polarization terms. However, use of a linearized code allows the selection of a mode with wavenumber justifying use of Eq. (28), i.e., $\omega_{pi}^2/k_\perp^2 c^2 = \beta_i/k_\perp^2 a_i^2 \gg (m_e/m_i)$, $(\omega_{ci}^2/\omega_{pi}^2)$ both of which are very small compared to unity for mirror plasmas ($\beta_i \equiv 8\pi n_0 T_i/B_0^2$). The neglect of the magnetic field gradient forfeits finite β_i corrections to the dispersion relation which are important for $\beta_i \gtrsim 1$ [13]. However, one of the more important corrections can be recovered by a renormalization of the plasma scale length, $L_n \to L_n[1 + \frac{1}{2}\beta_i(1 - T_e/T_i)]^{-1}$. We emphasize that the gradient of the equilibrium magnetic field has been omitted only for sake of simplicity and not as a prerequisite of the simulation model.

To simulate the drift-cone mode locally with our linearized canonical-momentum-conserving one-dimensional code, we artifically model the effect of the density gradient in the y direction but allow no variation of the fields and particle orbits in that direction. Therefore, canonical y-momentum is conserved within the local approximation. The direction of wave propagation is taken to be in the x-direction, and the magnetic field is in the z-direction. For sake of simplicity the electrons are again described as a cold, massless fluid. Hence the electron fluid velocity is given by $\mathbf{V}_e = c\mathbf{E} \times \hat{z}/B_0$. In the nonradiative and quasineutral limits, Ampere's law and $\nabla \cdot \mathbf{J} = 0$ become

$$k_x^2 \tilde{A}_y = 4\pi c^{-1}(\tilde{J}_y^{\,i} + en_0 \tilde{E}_x B_0^{-1} c), \tag{29}$$

$$ik_x(\tilde{J}_x^{\,i} - en_0 \tilde{E}_y B_0^{-1} c) + L_n^{-1}(\tilde{J}_y^{\,i} + en_0 \tilde{E}_x B_0^{-1} c)$$

$$= ik_x(\tilde{J}_x^{\,i} - en_0 \tilde{E}_y B_0^{-1} c) + (k_x^2 c/4\pi L_n)\,\tilde{A}_y = 0. \tag{30}$$

The electric field components $\tilde{E}_x$ and $\tilde{E}_y$ are obtained from solution of Eqs. (29) and (30). Analogous to Eqs. (7a), (7b), and (7c), the difference equations for the Fourier amplitudes of the fields become

$$\tilde{E}_x^{\,n} = (B_0/4\pi n_0 e)(k_x^2 \tilde{A}_y - 4\pi c^{-1} \tilde{J}_y^{\,i})^n, \tag{31a}$$

$$\tilde{E}_y^{\,n+1/2} = (B_0/4\pi n_0 e)[4\pi c^{-1}(\tilde{J}_x^{\,i})^{n+1/2} + (k_x^2/i\,2k_x L_n)(\tilde{A}_y^{\,n+1} + \tilde{A}_y^{\,n})], \tag{31b}$$

$$\tilde{A}_y^{(n+1)} = \tilde{A}_y^{(n)} + c\,\Delta t\,\tilde{E}_y^{\,n+1/2}. \tag{31c}$$

The dependence of Eq. (31b) on $\tilde{A}_y^{n+1}$ is resolved by simultaneous solution of Eqs. (31c) and (31b) for $\tilde{E}_y^{n+1/2}$ and $\tilde{A}_y^{n+1}$ as functions of $\tilde{A}_y^{\,n}$ and $(\tilde{J}_x^{\,i})^{n+1/2}$. After linearization, Eqs. (7c)-(8e) comprise the rest of the algorithm with one exception. In computing the ion charge and current densities, the individual particle ions are artificially weighted according to their initial y guiding center positions $y_{gc}(0)$ in a manner consistent with

the presumed density gradient, i.e., $e, m \propto \{1 + [y_{gc}(0) - y(t)]\, L_n^{-1}\}$. We remind the reader that the simulation model is local in y, independent of z, Fourier analyzed in x, and hence gridless.

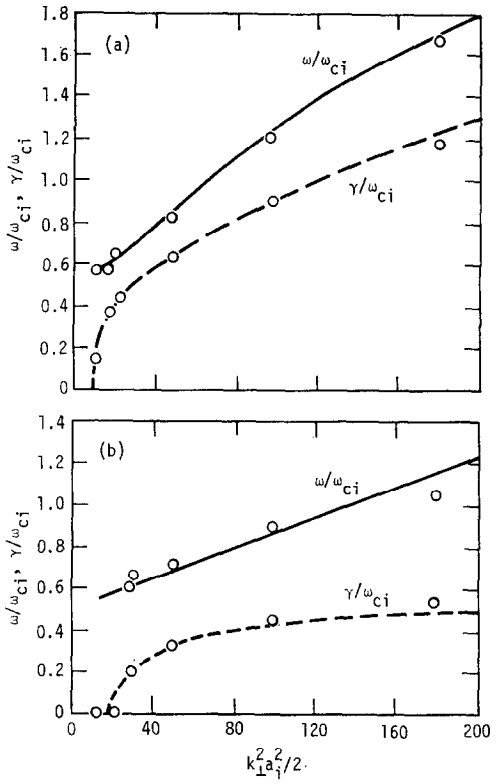

FIG. 5. Dispersion relation for the drift-cyclotron-loss-cone instability, $(\omega + i\gamma)/\omega_{ci}$ vs $k_\perp^2\, a_i^2/2$, with $T_e = 0$, $L_n/a_i = R = 10$, $\omega_{ci}\Delta t \leqslant 0.05$, and (a) $\beta_i = 0.1$ or (b) $\beta_i = 1.0$. The solid and dashed curves denote the predictions of analytical theory. The results of linearized simulations using the canonical-momentum-conserving algorithm are indicated by the data points.

Figure 5 shows the results of linearized simulations of the drift-cone mode for $\omega_{ci}\, \Delta t \leqslant 0.05$, $L_n/a_i = 10$, and $\beta_i = 0.1, 1$. We chose as the velocity distribution function the difference of two Maxwellians with a loss cone corresponding to an effective mirror ratio equal to 10. Increasing the value of β_i stabilizes the mode in agreement with theory [13, 19]. For the chosen values of $\omega_{ci}\, \Delta t$, there is little modification due to the finite time-step; the frequencies and growth rates observed in the simulations agree quite well with theory.

3. *Alfvén-Ion-Cyclotron Instability*

As a final example of microinstability we consider the Alfvén-ion-cyclotron mode, also known as the electromagnetic ion cyclotron instability. In a high-β plasma,

Alfvén-like waves can be destabilized by an ion energy anisotropy with $T_{i\perp} > T_{i\parallel}$. The most unstable waves propagate parallel to the magnetic field with frequency which satisfies $\omega \approx k_\parallel V_A \approx \omega_{ci}$. These modes are thought to play an important role in the energy isotropization of astrophysical plasmas with $T_{i\perp} > T_{i\parallel}$ and high-β laboratory plasmas heated by neutral-particle injection perpendicular to a confining magnetic field [11].

We follow the derivation by Davidson and Ogden [11] of the linear dispersion relation describing this instability. However, we assume that the electrons are cold and that electron polarization effects and the transverse displacement current are negligible. The latter assumptions are well justified for frequencies $\Omega \ll \omega_{ce}$, $k_\parallel c$. The dispersion relation becomes

$$0 = D^{\pm}(k_\parallel, \Omega \equiv \omega + i\gamma) = -k_\parallel{}^2 c^2 \mp \omega_{pe}^2 \Omega/\omega_{ce} + \omega_{pi}^2(\Omega/k_\parallel v_{i\parallel})\, Z(\xi_i^{\pm}) - \omega_{pi}^2(1 - T_{i\perp}/T_{i\parallel})[1 + \xi_i^{\pm} Z(\xi_i^{\pm})], \tag{32}$$

where the $\pm$ ($\mp$) labels refer to waves with right (left) circular polarization, $\xi_i^{\pm} = (\omega \pm \omega_{ci})/k_\parallel v_{i\parallel}$, $v_{i\parallel} = (2T_{i\parallel}/m_i)^{1/2}$, $T_{i\perp,\parallel} = \langle m_i v_{\perp,\parallel}^2 \rangle$, and $Z(\xi)$ is the plasma dispersion function

$$Z(\xi) \equiv (\pi)^{-1/2} \int_{-\infty}^{\infty} dx \exp(-x^2)/(x - \xi).$$

For purposes of one-dimensional simulation of the Alfvén-ion-cyclotron mode we take the direction of variation and the external magnetic field to be in z. Anticipating future studies of obliquely propagating Alfvén-ion cyclotron modes, we employ an algorithm which does not require conservation of canonical momentum, viz. we use the linearized predictor-corrector version of the leap-frog scheme, Eqs. (9), (10) and (11). For $\mathbf{k} = k_\parallel \hat{\mathbf{z}}$, only the z component of the particle position need be calculated. The zero order equations are

$$(d/dt)\, \mathbf{v}^{(0)} = (e/m_i)\, \mathbf{v}^{(0)} \times \mathbf{B}_0 c^{-1}$$
$$z = z_0 + v_z^{(0)} t.$$

The first order equations for the Fourier amplitudes become

$$k_\parallel{}^2(\tilde{A}_x \hat{\mathbf{x}} + \tilde{A}_y \hat{\mathbf{y}}) = 4\pi c^{-1}[(\tilde{J}_x{}^i + \tilde{J}_x{}^e)\, \hat{\mathbf{x}} + (\tilde{J}_y{}^i + \tilde{J}_y{}^e)\, \hat{\mathbf{y}}],$$
$$\tilde{J}_x{}^e \hat{\mathbf{x}} + \tilde{J}_y{}^e \hat{\mathbf{y}} = -en_0 c(\tilde{E}_x \hat{\mathbf{x}} + \tilde{E}_y \hat{\mathbf{y}}) \times \hat{\mathbf{z}} B_0^{-1}$$
$$-(\partial/c\, \partial t)(\tilde{A}_x \hat{\mathbf{x}} + \tilde{A}_y \hat{\mathbf{y}}) = \tilde{E}_x \hat{\mathbf{x}} + \tilde{E}_y \hat{\mathbf{y}},$$
$$\tilde{B}_x \hat{\mathbf{x}} + \tilde{B}_y \hat{\mathbf{y}} = ik_\parallel \hat{\mathbf{z}} \times (\tilde{A}_x \hat{\mathbf{x}} + \tilde{A}_y \hat{\mathbf{y}}),$$

$$(d/dt)(\tilde{v}_x \hat{\mathbf{x}} + \tilde{v}_y \hat{\mathbf{y}} + \tilde{v}_z \hat{\mathbf{z}}) = (e/m_i)[\tilde{E}_x \hat{\mathbf{x}} + \tilde{E}_y \hat{\mathbf{y}} + (\tilde{v}_x \hat{\mathbf{x}} + \tilde{v}_y \hat{\mathbf{y}} + \tilde{v}_z \hat{\mathbf{z}}) \times \mathbf{B}_0 c^{-1} + \mathbf{v}^{(0)} \times (\mathbf{B}_x \hat{\mathbf{x}} + \mathbf{B}_y \hat{\mathbf{y}} + \mathbf{B}_z \hat{\mathbf{z}})\, c^{-1}],$$
$$(d/dt)\, \tilde{z} = \tilde{v}_z.$$

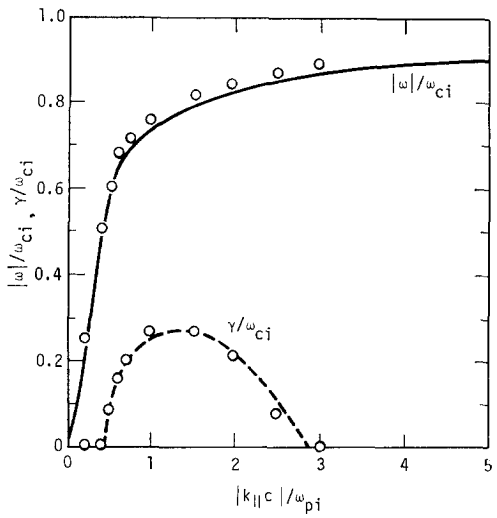

FIG. 6. Dispersion relation for the Alfvén-ion-cyclotron instability, $(|\omega| + i\gamma)/\omega_{ci}$ vs $|k_{||}c|/\omega_{pi}$, for $\beta_{i\perp} = 1$, $T_e = 0$, $T_{i\perp}/T_{i||} = 10$, and $\omega_{ci}\Delta t = 0.1$. The solid and dashed curves denote the predictions of analytical theory; the results of linearized simulation using the predictor-corrector scheme appear as data points.

These equations are numerically integrated in the manner of Eqs. (9), (10) and (11). Figure 6 displays the results of simulations for $\beta_{i\perp} \equiv 8\pi n_0 T_{i\perp}/B_0^2 = 1$, $\omega_{pi}^2/\omega_{ci}^2 \ll 1$, and $T_{i\perp}/T_{i||} = 10$. For $\omega_{ci}\Delta t = 0.1$ there is little effect due to finite-differencing in time. Alfvén-cyclotron modes are observed with polarizations, growth rates, and frequencies agreeing well with Davidson and Ogden's theoretical description and the solutions of Eq. (32). Linearized simulations with a spatial grid along $\mathbf{B}_0$ have shown that finite plasma length has a stabilizing influence on the Alfvén-ion-cyclotron mode in qualitative agreement with WKB theory [21, 22].

5. *Magnetic Field Cancellation and Electron Return Currents*

Another principal area of application of these simulation techniques is the study of neutral beam injection in high-β magnetically confined plasmas. Besides the issue of microinstability, recently much attention has been attracted by questions surrounding the creation of stable field-reversed magnetic-mirror configuration by means of neutral-particle injection perpendicular to the external magnetic field. Because a self-consistent model of large-orbit particle dynamics and the self-fields of the plasma is demanded for studying the approach to and the stability of field-reversed configurations, computer simulation is playing an important role in supporting analytical theory and experiments.

The efficiency of magnetic confinement in mirror plasmas can be substantially improved by increasing the depth of the magnetic well and hence increasing the mirror ratio. This can be achieved by creating a self-magnetic field in a direction opposite to

the external confining magnetic field; the self-field serves to locally cancel and perhaps even reverse the total magnetic field. Of course a single charged particle gyrating around a magnetic field line has a diamagnetic effect. The following simple argument illustrates how field cancellation depends on net plasma current within the context of the hybrid model presented in this paper.

The fluid equation of motion for electrons with negligible polarization drift and pressure is given by

$$0 = -ne(\mathbf{E} + \mathbf{V}_e \times \mathbf{B}c^{-1}) + nm_e(\mathbf{V}_i - \mathbf{V}_e)\,\nu_{ei}\,. \tag{33}$$

Note that this equation remains well-posed for $\mathbf{B} = 0$. If we take the curl of Eq. (33), use $\nabla \times \mathbf{E} = -c^{-1}\,\partial\mathbf{B}/\partial t$, assume conditions such that $|\,\nabla\nu_{ei} \times \nabla^2\mathbf{A}\,| \ll |\,\nu_{ei}\nabla^2\mathbf{B}\,|$, and neglect the transverse displacement current, then

$$\begin{aligned}\partial B_z/\partial t = {} & -(ne)^{-1}\,[B_z(\nabla \cdot \mathbf{J}^e) - (\mathbf{B} \cdot \nabla)\,J_z^e - (\mathbf{J}^e \cdot \nabla)\,B_z] \\ & + (\nu_{ei}/\omega_{pe}^2)\,c^2\,\nabla^2 B_z + c\hat{z} \cdot (\nabla \ln n \times \mathbf{E}).\end{aligned} \tag{34}$$

We examine Eq. (34) near a minimum of B_z at the midplane of a magnetic mirror, and for sake of simplicity we assume azimuthal symmetry ($\partial/\partial\theta = 0$). In the limit that the minimum of B_z approaches zero, Eq. (34) becomes

$$\partial B_z/\partial t \approx (\nu_{ei}/\omega_{pe}^2)\,c^2\,\nabla^2 B_z + cE_\theta\,\partial \ln(n)/\partial r. \tag{35}$$

E_θ satisfies the equation $\nabla^2 E_\theta = -\partial\nabla^2 A_\theta/c\,\partial t = (4\pi/c^2)\,\partial J_\theta/\partial t$, with boundary conditions $E_\theta = 0$ at $r = 0$ and $r = \infty$. The first term on the right side of Eq. (35) tends to smooth extrema on the magnetic field: it is positive at a minimum and negative at a maximum. The second term on the right can drive the cancellation of the magnetic field; without this term there can be no field depression to a null. To see this, choose $B_z\,(t = 0) > 0$. Consider what happens as a diamagnetic current builds up. For reasonable density profiles, and J_θ increasingly negative in time over a spatial domain, the product of the induced electric field E_θ and the density gradient can be negative locally in space. For a ring current, a field null can be achieved inside the ring for a plasma density with a local maximum at a smaller radius or on axis.

In order that there be substantial generation of a self-magnetic field, there must evidently be an appreciable plasma current. A potential threat to achieving field reversal is the emergence of plasma return currents which cancel the ion currents produced by neutral-beam injection and the subsequent charge-exchange and collisional ionization of the beam. Berk and Pearlstein have analytically calculated the plasma return currents for parallel and perpendicular external currents embedded in a magnetized plasma whose response is taken to satisfy the zero temperature magnetohydrodynamic equation and Ohm's law [23]. The prescribed external current is assumed small so that a linear analysis can be performed. They find that only for a period of time less than or equal to the perpendicular Alfvén transit time of the

system after initiation of the embedded current does a return current cancel the perpendicular external current.

Berk and Pearlstein's results can be understood as follows. Consider an embedded current sheet with magnitude that rises linearly in time, $I_s = \kappa t$. In an initially undisturbed plasma confined between conducting walls, the information that there is a rising current transverse to the magnetic field is carried by a compressional Alfvén wave. Ahead of this wave the fluid remains unperturbed. Behind the wave, $-V_A t < x < V_A t$, there is a constant current density of magnitude $J_y(x, t) = -\kappa/2V_A$ whose integrated current is equal and opposite to the imposed current. Berk and Pearlstein find that this consequence of the linearized *MHD* equations is valid at early times before the waves reflect at the plasma boundaries. The situation is sketched in Fig. 7.

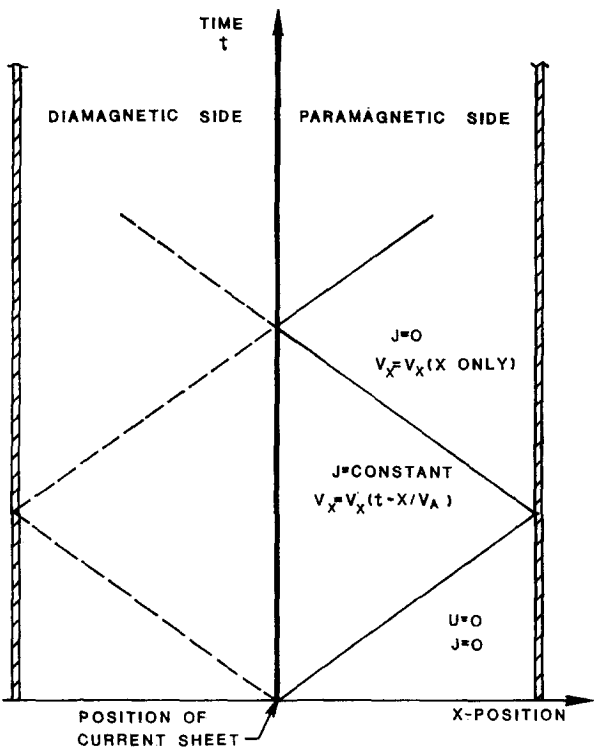

FIG. 7. Space-time diagram for Berk-Pearlstein wave. The wave is a compressional perturbation of magnetic field lines on the paramagnetic side and a rarefaction on the diamagnetic side.

With a constant current density, the fluid velocity will vary linearly in time, since $\rho_0(\partial V_x/\partial t) = J_y B_0 c^{-1}$ in the linear approximation. The magnetic field of the wave at any instant will consist of a linear decrease from the unperturbed value at the wavefront on the "diamagnetic" side of the embedded current, followed by a jump upwards at the current sheet, and then a linear decrease back to the unperturbed value at the opposite traveling wavefront on the "paramagnetic" side. (For axisymmetric ion or

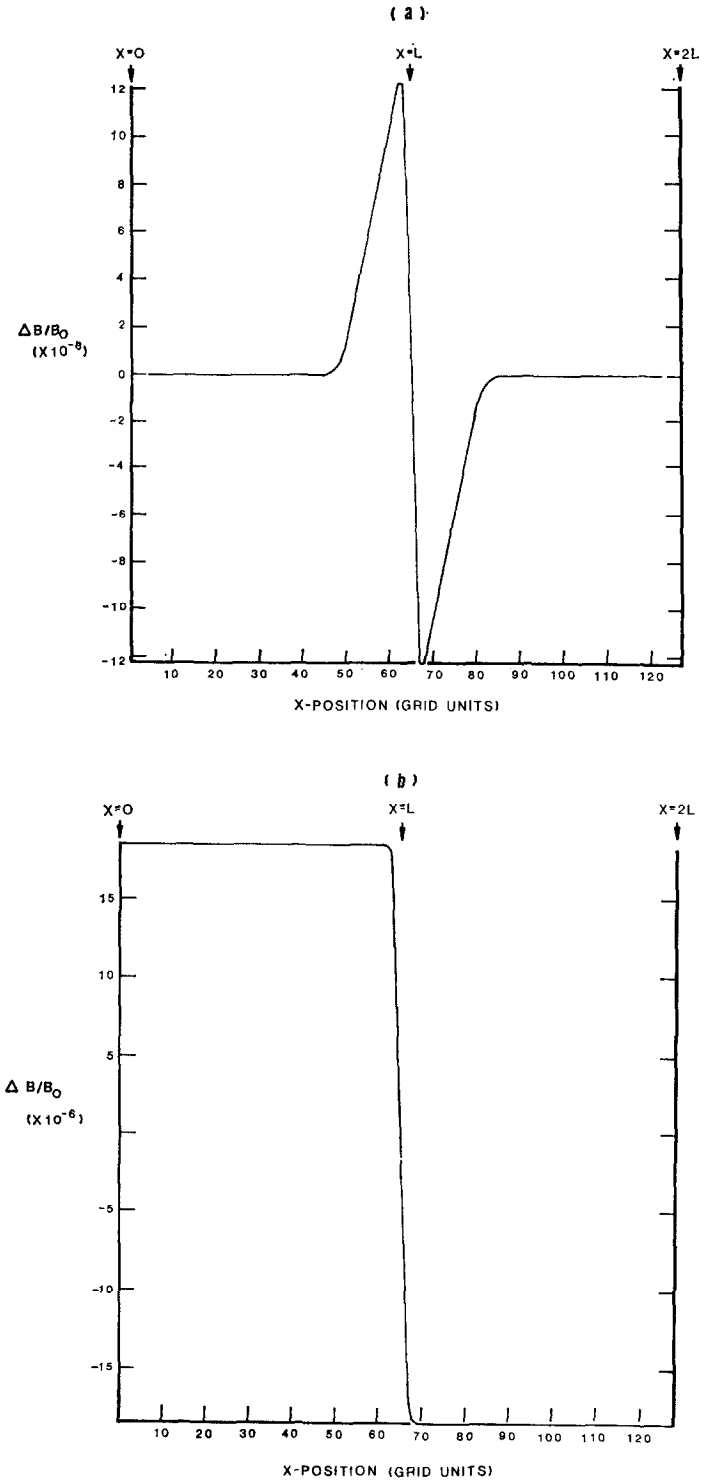

FIG. 8. Simulated instantaneous magnetic field perturbations versus position at (a) early times showing the effects of current cancelling electron return currents and (b) late times after electron return currents have subsided.

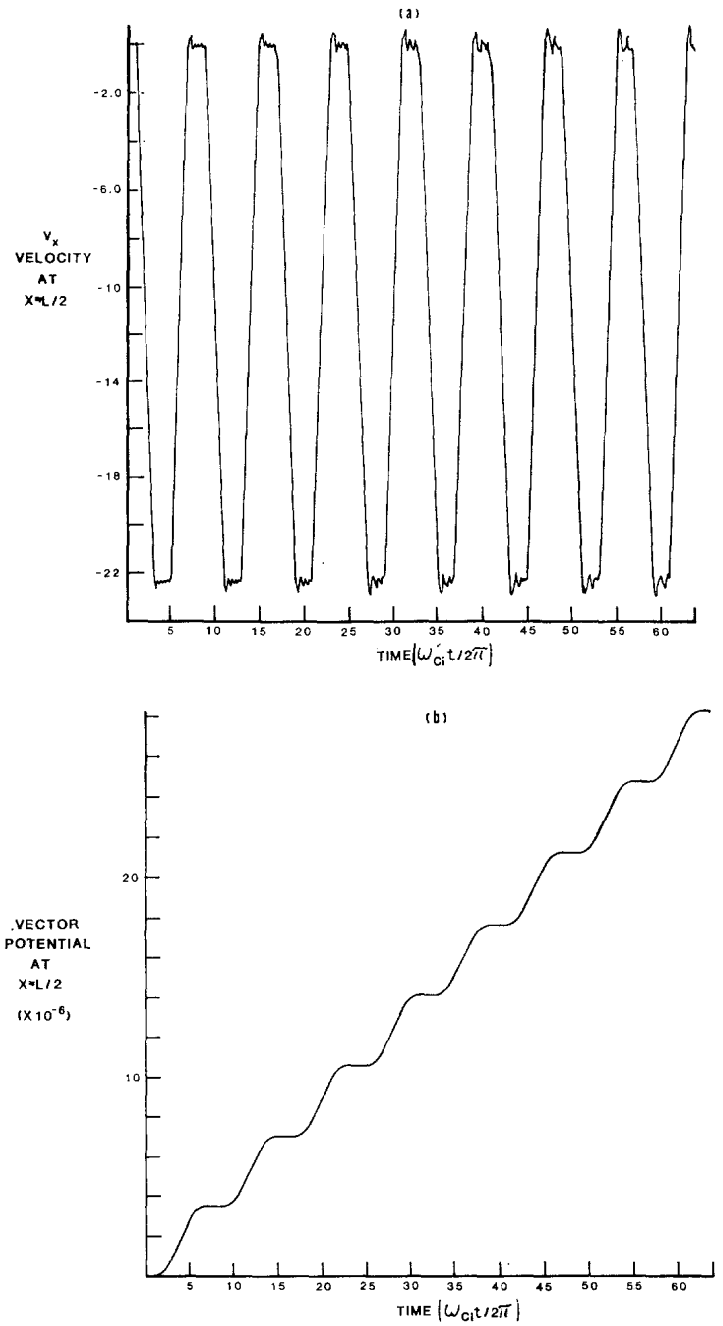

FIG. 9. At $x = L/2$, a position midway between the current and the wall on the diamagnetic side are plotted (a) the plasma velocity V_x, (b) the vector potential A_y, and (c) the plasma current J_y versus time, $\omega_{ci}t/2\pi$, for the Pearlstein-Berk wave.

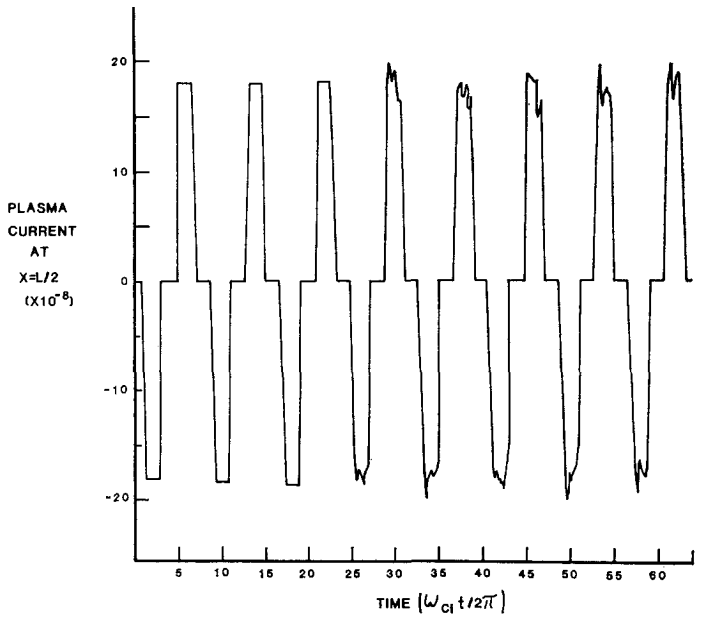

FIG. 9—*Continued*

electron current rings, the diamagnetic side is always the inside of the ring.) Only after the compressional Alfvén waves have suffered many reflections and interfered with one another over many Alfvén transit times of the system does the electron return current subside and does a self-field build up.

We have tested the results of simulations with our canonical momentum-conserving algorithm, Eqs. (7) and (8), against the predictions of Berk and Pearlstein in slab geometry with weak perturbations of the magnetic field, $\Delta B/B_0 \leqslant 2 \times 10^{-5}$. A plot of the instantaneous magnetic field at early time is shown in Fig. 8a. The self-field of the plasma is seen to have roughly the predicted triangular shape, but with rounded peaks and rounded feet. These features are due to the numerical dispersion arising from the space-time mesh. The magnetic field at a time after many wave reflections have occurred is shown in Fig. 8b and has the characteristics to be expected for negligible plasma return current as predicted by Berk and Pearlstein.

There is a slight difference between the physical circumstances of these simulations and the situation considered by Berk and Pearlstein. The simulations have included the $\mathbf{E} \times \mathbf{B}$ dynamics of charge neutralizing electrons which accompany the injected ions and were neglected in [23]. These electrons are given the same narrow spatial profile as the external current. For injected densities less than one-tenth the background plasma density, the plasma response is insensitive to the extra electrons. The embedded ion current is spread over three simulation cells compared to the total plasma length $2L$ of 64 cells. Berk and Pearlstein assumed an embedded current of negligible thickness.

A time history of the plasma velocity at a point midway between the current sheet and the wall is shown in Fig. 9. The finite time $L/2\ V_A$ for the compressional Alfvén wave to reach this position, followed by the initial linear velocity rise, is clearly visible. During this time the vector potential rises quadratically in time. At a time L/V_A later the reflected wave returns to this position. Behind this wave, $J_y = 0$ from the boundary condition that there be no acceleration of fluid into the wall. This means that V_x and E_y are constants at any point in space between the wall and the reflected wave. Thus the vector potential should rise linearly with time until another wave reflected from the current sheet returns. The expected behavior of the fluid velocity is seen between $3 \leqslant \omega_{ci}t/2\pi \leqslant 5$ in Fig. 9a, and the quadratic variation ($1 \leqslant \omega_{ci}t/2\pi \leqslant 3$) and linear variations of the vector potential are shown in Fig. 9b.

A plot of the plasma current versus time at $x = L/2$ is shown in Fig. 9c. High frequency noise at high cyclotron frequency harmonics has been filtered out of this trace. The important point is that the plasma current continues to grow. The oscillation period has been verified to be $2L/V_A$ within 2% . Because of the numerical wave dispersion (Fig. 3), some discrepancy is to be expected. The cumulative effect of dispersion on integrated quantities such as the vector potential is negligible over the times considered ($\omega_{ci}t/2\pi = 64$ with $\omega_{ci}\,\Delta t = 0.2$). For other quantities, such as the x velocity and y current, the dispersion and noise build up to appreciable, but tolerable, levels. In general, the simulation results agree quite well with analytical theory and demonstrate that an ion current perpendicular to the external magnetic field and a concomitant diamagnetic self-field can be established.

6. Conclusions

In this paper we have presented a new class of algorithms for performing computer simulations of collective plasma behavior at low frequencies. Electrons are represented as a fluid and the ions as particles. Maxwell's equations are solved with the transverse displacement current ignored and quasineutrality assumed. Stability of our various numerical schemes generally demands that $(kV_A\,\Delta t)_{\text{eff}} \lesssim 1$ and that $\omega_{ci}\,\Delta t \lesssim 1$, where the effective Alfvén frequency $(kV_A)_{\text{eff}}$ includes modifications due to the space-time mesh. Our algorithms are remarkably simple and direct.

We find our simulations to be fairly efficient. A typical one-dimensional nonlinear simulation with 128 spatial grid cells requires 25×10^{-6} sec per particle per time step for all operations exclusive of input and output on the National Magnetic Fusion Energy Computer Center *CDC* 7600. A typical one-dimensional linearized simulation using the predictor-corrector version of the leap-frog method is much slower, 120×10^{-6} sec per particle per time step. This is because this algorithm must integrate both zero and first order equations once each time step for the predictor step and then again for the corrector iteration.

We have used the propagation of small amplitude compressional Alfvén waves in cold plasma to provide understanding and tests of the various algorithms. Our simulations agree extremely well with the results of anlytical theory which includes

significant effects due to finite differencing. We have also performed linearized simulations of three microinstabilities: two essentially electrostatic modes, the Dory-Guest-Harris instability and the drift-cyclotron-loss-cone mode; and the Alfvén-ion-cyclotron mode which is electromagnetic. Finite-differencing effects are small in these simulations, and the simulation results agree with linear analytical theory. The generally stabilizing influence of the electromagnetic modifications of the dominantly electrostatic modes is an important feature which our simulations quite easily demonstrate. We have reprted elsewhere on simulations of the Alfvén-ion-cyclotron mode in which finite plasma effects have a stabilizing effect [21]. To the best of our knowledge, simulations of the drift-cyclotron-loss-cone mode, including electromagnetic effects, and the Alfvén-ion-cyclotron mode have not previously been presented in the literature[1]. In the future, we expect to extend study of these microinstabilities to higher dimensions and fully nonlinear investigations, and include finite geometry effects.

We have also described the application of these simulation models to the study of field-reversed magnetic-mirror configurations. Our simulations have verified the results of Berk and Pearlstein describing the transient plasma response to a growing, small amplitude, embedded external current which is perpendicular to the external magnetic field. Electron return currents effectively cancel the external current only for times up to Alfvén transit time of a plasma confined between conducting walls, after which there is growth of net current and accompanying magnetic field modification. The extension of these studies to the simulation of a cylindrical $(r - z)$ reversed magnetic field configuration is under way.

APPENDIX 1: DIRECT INTEGRATION METHOD FOR E AND B

Drs. J. Denavit and A. Friedman brought to our attention a variation of our general multidimensional algorithms (leap-frog, implicit, and predictor-corrector schemes) which offers a significant economy in computation. Equations (9) in the text are replaced by

$$\tfrac{1}{2}(\mathbf{E}^{n+1} + \mathbf{E}^n) = [\omega_{pi}^{-2} c(\nabla \times \mathbf{B}) \times \boldsymbol{\omega}_{ci} - (nec)^{-1} \mathbf{J} \times \mathbf{B} - (ne)^{-1} \nabla \cdot \mathbf{P}_e + \nu_{ei} \omega_{pe}^{-2} c(\nabla \times \mathbf{B})]^{n+1/2},$$

$$\mathbf{B}^{n+1/2} = \mathbf{B}^{n-1/2} - c\,\Delta t\, \nabla \times \mathbf{E}^n,$$

$$\mathbf{B}^n = \tfrac{1}{2}(\mathbf{B}^{n+1/2} + \mathbf{B}^{n-1/2}).$$

This eliminates the vector potential **A** as a variable and the necessity of separating $\mathbf{E}^t$ and $\mathbf{E}^l$ (taking the curl of the electric field annihilates $\mathbf{E}^l$ in Faraday's law). A savings of computer memory and operations count is thus achieved in the leap-frog and predictor-corrector simulation codes.

[1] *Note added in proof.* Subsequent to the first submittal of this article, simulations of the Alfvén-ion-cyclotron mode were discussed by T. Tajima, K. Mima, and J. M. Dawson, *Phys. Rev. Lett.* **39** (1977), 201.

However, these modifications do not fundamentally alter the structure of the field equations. The order of spatial differentiation is preserved with $-\nabla \times \mathbf{B}$ replacing $\nabla^2\mathbf{A}$ in Eq. (9a) and by taking the curl of Eq. (9c). In performing the linear stability analysis, we obtain the same dispersion relations as are found in Section 3 except that K^2 appearing in Eqs. (18), (21), (22) and (23) is now given by $K^2 \equiv k^2 \sin^2(k\,\Delta x)/(k\,\Delta x)^2$. This arises due to spatial grid effects, namely that $D^2 \neq (D^1)^2$. As a result there is a larger grid effect for the same value of $k\,\Delta x$ as compared with the algorithms in the text for which $K^2 \equiv k^2 \sin^2(k\,\Delta x/2)/(k\,\Delta x/2)^2$.

APPENDIX 2: NUMERICAL STABILITY ANALYSIS FOR A WARM PLASMA

In this appendix we present a kinetic description of the waves propagating across the magnetic field in a warm homogeneous plasma as simulated by our one-dimensional, canonical-momentum-conserving algorithm, Eqs. (7) and (8). In terms of Fourier amplitudes, the linearized Maxwell's equations, Eqs. (7), are

$$\frac{-i\omega_{pi}^2}{\omega\omega_{ci}} \frac{\sin(\omega\,\Delta t/2)}{\omega\,\Delta t/2} \frac{i\omega}{c} \tilde{A}_y + \frac{4\pi i}{\omega} \tilde{J}_x^{(1)} = 0, \tag{A1}$$

$$\frac{i\omega_{pi}^2}{\omega\omega_{ci}} \tilde{E}_x - \frac{K^2c^2}{\omega^2} \frac{i\omega}{c} \tilde{A}_y + \frac{4\pi i}{\omega} \tilde{J}_y^{(1)} = 0. \tag{A2}$$

The linearized ion current $\mathbf{J}^{(1)}$ must be determined from the first order velocity and density perturbations.

The zero order equations of motion deduced from Eqs. (8) are Fourier transformed in time to obtain

$$\tilde{v}_y^{(0)} = -\omega_{ci}\tilde{x}^{(0)}, \tag{A3a}$$

$$-i \frac{\sin(\Omega\,\Delta t/2)}{\omega_{ci}\,\Delta t/2} \tilde{v}_x^{(0)} = \eta\tilde{v}_y^{(0)}, \tag{A3b}$$

$$-i \frac{\sin(\Omega\,\Delta t/2)}{\omega_{ci}\,\Delta t/2} \omega_{ci}\tilde{x}^{(0)} = \eta\tilde{v}_x^{(0)}, \tag{A3c}$$

where the effective cyclotron frequency Ω is given by $\sin(\Omega\,\Delta t/2) = \eta\omega_{ci}\,\Delta t/2$. For choice $\eta = \sin(\omega_{ci}\,\Delta t/2)/(\omega_{ci}\,\Delta t/2)$, the ions gyrate with the correct frequency $\Omega = \omega_{ci}$. Hence $v_x^{(0)} = v_\perp \cos(\phi - \Omega t)$, $v_y^{(0)} = v_\perp \sin(\phi - \Omega t)$, and $x^{(0)} = x_c - (v_\perp/\omega_{ci}) \sin(\phi - \Omega t)$, where ϕ is the initial gyrophase and x_c is the guiding center location. Then use of a Bessel function identity gives

$$\exp(-i\omega t + ikx^{(0)}) = \exp(ikx_c) \sum_r J_r(kv_\perp/\Omega) \exp[-ir\phi - i\omega_r t], \tag{A4}$$

where $\omega_r \equiv \omega - r\Omega$.

The essence of the method of characteristics is the evaluation of the phase of the

$$A_y, E_x = (A_y, E_x) \exp(-i\omega t + ikx) + c.c. \approx (A_y, E_x) \exp(-i\omega t + ikx^{(0)}) + \text{c.c.} \tag{A5}$$

Equation (A4) is then used to represent the perturbed fields with respect to $\exp(-i\omega_r t)$. We represent the orbit modifications similarly, i.e. $v_x^{(1)}, v_y^{(1)}, x^{(1)} = \sum_r (\tilde{v}_x{}^r, \tilde{v}_y{}^r, \tilde{x}^r) \exp(-i\omega_r t) + c.c.$. Using Eqs. (8) and (A5), we obtain after some algebra

$$\tilde{v}_x{}^r = \frac{i(\eta\omega_{ci}\,\Delta t/2)\sin(\omega_r\,\Delta t/2)}{(\eta\omega_{ci}\,\Delta t/2)^2 - \sin^2(\omega_r\,\Delta t/2)}\,\tilde{S}\exp(ikx_c - ir\phi)$$

$$\times\left[\omega_{ci}J_r\frac{\tilde{A}_y}{B_0} - cJ_r\frac{\tilde{E}_x}{B_0} - \frac{kv_\perp}{2}\frac{\sin(k\,\Delta x)}{k\,\Delta x}(J_{r-1} - J_{r+1})\frac{\tilde{A}_y}{B_0}\right], \tag{A6a}$$

$$\tilde{v}_y{}^r = -\omega_{ci}\tilde{S}J_r\exp(ikx_c - ir\phi)\frac{\tilde{A}_y}{B_0} + \frac{(\eta\omega_{ci}\,\Delta t/2)^2}{(\eta\omega_r\,\Delta t/2)^2 - \sin^2(\omega_r\,\Delta t/2)}\,\tilde{S}\exp(ikx_c - ir\phi)$$

$$\times\left[\omega_{ci}J_r\frac{\tilde{A}_y}{B_0} - cJ_r\frac{E_x}{B_0} - \frac{kv_\perp}{2}\frac{\sin(k\,\Delta x)}{k\,\Delta x}(J_{r-1} - J_{r+1})\frac{\tilde{A}_y}{B_0}\right], \tag{A6b}$$

and

$$\tilde{x}^r = -\frac{(\eta\omega_{ci}\,\Delta t/2)^2}{(\eta\omega_{ci}\,\Delta t/2)^2 - \sin^2(\omega_r\,\Delta t/2)}\,\tilde{S}\exp(ikx_c - ir\phi)$$

$$\times\left[J_r\frac{\tilde{A}_y}{B_0} - \frac{c}{\omega_{ci}}J_r\frac{\tilde{E}_x}{B_0} - \frac{kv_\perp}{2\omega_{ci}}\frac{\sin(k\,\Delta x)}{k\,\Delta x}(J_{r-1} - J_{r+1})\frac{\tilde{A}_y}{B_0}\right],$$

where the argument of the Bessel functions is given by $kv_\perp/\Omega$.

The perturbed ion currents to first order in perturbed fields can now be calculated according to Eq. (8b) and are given by

$$J_x^{(1)} = en_0\tilde{S}\int d^3v\, g_0(\mathbf{v})\Big\{v_x^{(1)}\exp(-i\omega t + ikx^{(0)})$$

$$+ (\tilde{n}^{(1)}/n_0)\frac{v_x^{(0)}}{2}[\exp(-i\omega t + i\omega\,\Delta t/2 + ikx_{-1/2}^{(0)})$$

$$+ \exp(-i\omega t - i\omega\,\Delta t/2 + ikx_{1/2}^{(0)})]\Big\} + \text{c.c.} \tag{A7a}$$

and

$$J_y^{(1)} = en_0\tilde{S}\int d^3v\, g_0(\mathbf{v})[\tilde{v}_y^{(1)} + (\tilde{n}^{(1)}/n_0)\,v_y^{(0)}]\exp(-i\omega t + ikx^{(0)}) + \text{c.c.}, \tag{A7b}$$

where $x^{(0)} = x_c - (v_\perp/\omega_{ci})\sin(\phi - \Omega t)$ and $x_{\pm 1/2}^{(0)} = x_c - (v_\perp/\omega_{ci}) \times \sin(\phi - \Omega t \pm \Omega\,\Delta t/2)$ and $n^{(1)} = -n_0\,\partial x^{(1)}/\partial x^{(0)}$ [3]. We next use the expressions for $v_x^{(0)}$ and $v_y^{(0)}$ obtained earlier, and substitute $\exp(ikx_c) = \exp(ikx)\sum_{r'} J_{r'}(kv_\perp/\Omega)\exp(ir'\phi - ir'\,\Omega t)$. We employ the relation $\int d\phi\exp[i(l-m)\phi] = 2\pi\,\delta_{lm}$ in performing the

velocity space integrations. The Fourier transformed perturbed ion currents are thus

$$\tilde{J}_x^{(1)} = en_0\tilde{S}^2 \int dv_\perp\, v_\perp g_0(v_\perp) \sum_r \Bigg[\frac{i \sin(\omega_r\, \Delta t/2)(\eta\omega_{ci}\, \Delta t/2)}{(\eta\omega_{ci}\, \Delta t/2)^2 - \sin^2(\omega_r\, \Delta t/2)}$$
$$\times \left\{-cJ_r{}^2 \frac{\tilde{E}_x}{B_0} + \left[\frac{kv_\perp}{2} \frac{\sin(k\, \Delta x)}{k\, \Delta x} (J_{r+1}J_r - J_{r-1}J_r) + \omega_{ci}J_r{}^2\right] \frac{\tilde{A}_y}{B_0}\right\}$$
$$+ \frac{i(kv_\perp/2\omega_{ci})(\eta\omega_{ci}\, \Delta t/2)^2}{(\eta\omega_{ci}\, \Delta t/2)^2 - \sin^2(\omega_r\, \Delta t/2)} \cos(\omega_r\, \Delta t/2)$$
$$\times \left\{-J_r(J_{r-1} + J_{r+1})\, c \frac{\tilde{E}_x}{B_0} + \left[\frac{kv_\perp}{2} \frac{\sin(k\, \Delta x)}{k\, \Delta x} (J_{r+1} - J_{r-1})(J_{r+1} + J_{r-1})\right.\right.$$
$$\left.\left. + \omega_{ci}J_r(J_{r-1} + J_{r+1})\right] \frac{\tilde{A}_y}{B_0}\right\}\Bigg] \tag{A8a}$$

and

$$\tilde{J}_y^{(1)} = en_0\tilde{S}^2 \int dv_\perp\, v_\perp g_0(v_\perp) \sum_r \Bigg[-\omega_{ci}J_r{}^2 \frac{\tilde{A}_y}{B_0} + \frac{(\eta\omega_{ci}\, \Delta t/2)^2}{(\eta\omega_{ci}\, \Delta t/2)^2 - \sin^2(\omega_r\, \Delta t/2)}$$
$$\times \left\{-cJ_r{}^2 \frac{\tilde{E}_x}{B_0} + \left[\omega_{ci}J_r{}^2 + \frac{kv_\perp}{2} \frac{\sin(k\, \Delta x)}{k\, \Delta x} J_r(J_{r+1} - J_{r-1})\right] \frac{\tilde{A}_y}{B_0}\right\}$$
$$+ \frac{(\eta\omega_{ci}\, \Delta t/2)^2\, (kv_\perp/2\omega_{ci})}{(\eta\omega_{ci}\, \Delta t/2)^2 - \sin^2(\omega_r\, \Delta t/2)} \left\{-cJ_r(J_{r-1} - J_{r+1}) \frac{\tilde{E}_x}{B_0}\right.$$
$$\left. + \left[\omega_{ci}J_r(J_{r-1} - J_{r+}) + \frac{kv_\perp}{2} \frac{\sin(k\, \Delta x)}{k\, \Delta x} (J_{r+1} - J_{r-1})(J_{r-1} - J_{r+1})\right] \frac{\tilde{A}_y}{B_0}\right\}\Bigg]. \tag{A8b}$$

Substitution of Eqs. (A8) into Eqs. (A1) and (A2) gives Eqs. (24) and (25) in the main body of the paper.

We observe that, due to using the particular interpolation and averaging procedure for J_x indicated in Eq. (8b), there appears in Eq. (A8a) the factor $\cos(\omega_r\, \Delta t/2)$. This leads to appreciable smoothing for $\omega_r\, \Delta t/2 \sim \pi/2$ and to a change in sign of the plasma current contributed by the rth cyclotron harmonic component of $n^{(1)}\, ev_x^{(0)}$ for particular values of r.

If Eq. (8b) for J_x were replaced by

$$J_x(x_j)^{n+1/2} = \sum_i S[x_j - \tfrac{1}{2}(x_i{}^n + x_1^{n+1})]\, ev_{x,i}^{n+1/2},$$

then Eq. (A7a) would become

$$J_x^{(1)} = en_0\tilde{S} \int d^3v\, g_0(\mathbf{v})\{\tilde{v}_x^{(1)} \exp(-i\omega t + ikx^{(0)})$$
$$+ (\tilde{n}^{(1)}/n_0)\, v_x^{(0)} \exp[-i\omega t + ik(x_{1/2}^{(0)} + x_{-1/2}^{(0)})/2]\} + \text{c.c.}$$

In Eqs. (A8a) and (25) the multiplicative factor $\cos(\omega_r \Delta t/2)$ would consequently be replaced by unity, and the argument of the first Bessel function appearing in the products of Bessel functions in all terms immediately following would be renormalized, $kv_\perp/\Omega \to \cos(\Omega \Delta t/2)\, kv_\perp/\Omega$. This would produce a different smoothing of the cyclotron harmonic components.

ACKNOWLEDGMENTS

We wish to thank Drs. C. K. Birdsall, J. Denavit, A. Friedman, D. W. Hewett, A. B. Langdon, L. D. Pearlstein, and D. C. Watson for many useful discussions, assistance, and encouragement. We also thank the referees for their helpful suggestions which have improved the content of this paper.

REFERENCES

1. C. G. DARWIN, *Phil. Mag.* **39** (1920), 537.
2. A. N. KAUFMAN AND P. S. ROSTLER, *Phys. Fluids* **14** (1971), 446.
3. A. B. LANGDON, *in* "Proceedings of the Fourth Conference on Numerical Simulation of Plasmas" (J. P. Boris and R. Shanny, Eds.), p. 467, U.S. Government Printing Office, Washington, D.C., 1970.
4. C. W. NIELSON AND H. R. LEWIS, *in* "Methods in Computational Physics" (J. Killeen, Ed.), Vol. 16, p. 367, Academic Press, New York, 1976.
5. A. HASEGAWA AND H. OKUDA, *Phys. Fluids* **11** (1968), 1995.
6. I. HABER, C. E. WAGNER, J. P. BORIS, AND J. M. DAWSON, *in* "Proceedings of the Fourth Conference on Numerical Simulation of Plasmas" (J. P. Boris and R. Shanny, Eds.), p. 126, U.S. Government Printing Office, Washington, D.C., 1970.
7. J. BUSNARDO-NETO, P. L. PRITCHETT, A. T. LIN, AND J. M. DAWSON, *J. Computational Phys.* **23** (1977), 300.
8. C. W. NIELSON, D. WINSKE, AND D. W. HEWETT, *in* "Proceedings of the Annual CTR Theory Meeting," 2A-17, University of Wisconsin, Madison, 1976.
9. A. FRIEDMAN, R. L. FERCH, R. N. SUDAN, AND A. T. DROBOT, "Numerical Simulation of Strong Proton Rings," Laboratory of Plasma Studies Report No. 190, Cornell University, October 1976.
10. R. A. DORY, G. E. GUEST, AND E. G. HARRIS, *Phys. Rev. Lett.* **14** (1965), 131.
11. R. C. DAVIDSON AND J. M. OGDEN, *Phys. Fluids* **18** (1975), 1045.
12. A. B. MIKHAILOVSKII, *Nucl. Fusion* **5** (1965), 125.
13. W. M. TANG, L. D. PEARLSTEIN, AND H. L. BERK, *Phys. Fluids* **15** (1972), 1153.
14. D. FUSS AND C. K. BIRDSALL, *J. Computational Phys.* **3** (1969), 494.
15. J. P. BORIS, *in* "Proceedings of the Fourth Conference on Numerical Simulation of Plasmas" (J. P. Boris and R. Shanny, Eds.), p. 3, U.S. Government Printing Office, Washington, D.C., 1970.
16. A. B. LANGDON AND B. F. LASINSKI, *in* "Methods in Computational Physics" (J. Killeen, Ed.), Vol. 16, p. 327, Academic Press, New York, 1976.
17. J. P. FREIDBERG, R. L. MORSE, AND C. W. NIELSON, *in* "Proceedings of the Third Conference on Numerical simulation of Plasmas," 15, Stanford University, 1969.
18. J. A. BYERS, *in* "Proceedings of the Fourth Conference on Numerical Simulation of Plasmas" (J. P. Boris and R. Shanny, Eds.), p. 496, U.S. Government Printing Office, Washington, D.C., 1970.

19. J. D. CALLEN AND G. E. GUEST, *Phys. Fluids* **14** (1971), 1588.
20. F. W. CRAWFORD AND J. A. TATARONIS, *J. Appl. Phys.* **36** (1965), 2930.
21. J. A. BYERS, *in* "Proceedings of the Annual CTR Theory Meeting," P-2, University of Wisconsin, Madison, 1976.
22. L. D. PEARLSTEIN, D. C. WATSON, AND L. L. LODESTRO, in *Bull. Amer. Phys. Soc.* **21** (1976), 1106.
23. H. L. BERK AND L. D. PEARLSTEIN, *Phys. Fluids* **19** (1976), 1831.